State-to-State Transport in Hypersonic Entry Flows

Ana Catarina Garbacz Gomes

Thesis to obtain the Master of Science Degree in

Aerospace Engineering

Supervisors: Prof. Mário António Prazeres Lino da Silva
Dr. Maria Luís Grácio Bilro Castela

Examination Committee

Chairperson: Prof. Fernando José Parracho Lau
Supervisor: Prof. Mário António Prazeres Lino da Silva
Member of the Committee: Prof. José Manuel da Silva Chaves Ribeiro Pereira

September 2018

Acknowledgments

Undertaking this thesis would not have been possible without the support and guidance that I received from many people.

First of all, I would like to express my great appreciation to Professor Mário Lino da Silva, for accepting to be my supervisor and for providing me with the opportunity to tackle considerable challenges in the field of high-temperature gas dynamics. His guidance and immense knowledge were crucial throughout the developement of this project. I would also like to express my deep gratitude to my co-supervisor, Dr. Maria Castela, not only for her endless patience and technical support but mainly for her advice on how to approach problems in an effective way. My grateful thanks are also extended to Dr. Bruno Lopez, from the University of Illinois in Urbana-Champaign, who provided insight into the subject and technical support regarding the SPARK code.

I thank all my friends for their advice and constant support.

Last but not least, I would like to thank my family for making this possible and for encouraging me to always challenge myself and set ambitious goals. I dedicate this thesis to you.

Resumo

O presente trabalho propõe-se a analisar escoamentos hipersónicos em desequilíbrio, em torno de veículos de entrada atmosférica. O desenho destes veículos e dos respectivos sistemas de proteção térmica requere a modelação adequada dos fenómenos de transporte a alta temperatura. Nesta tese, os processos de dissociação e de relaxação para a transferência de energia vibracional são tratados utilizando uma abordagem cinética *state-to-state*. Um estudo numérico do escoamento de azoto a alta velocidade em torno de uma esfera foi realizado com o objectivo de avaliar o impacto da implementação de coeficientes de transporte numa abordagem *state-to-state*, no código SPARK. Duas aproximações foram consideradas utilizando o modelo Gupta-Yos: uma transposição directa das propriedades de transporte macroscópicas para cada estado interno, e a mesma transposição multiplicada por um factor correctivo, considerando o aumento das secções de colisão para moléculas vibracionalmente excitadas. Consideraram-se vários modelos aerotermodinâmicos: Euler state-to-state, e Navier-Stokes *state-to-state*, uma-temperatura e duas-temperaturas. A inclusão de fenómenos de transporte na abordagem *state-to-state* (Navier–Stokes vs. Euler) resultou em variações das propriedades do escoamento mais suaves, o que se traduziu num pico de temperatura 15% inferior com uma posição do choque aproximadamente igual. Comparando a simulação Navier-Stokes *state-to-state* com a simulação a duas-temperaturas, a primeira abordagem resultou num choque mais afastado da parede e num pico de temperature superior, em 10% e 5%, respectivamente. Contudo, o impacto do modelo State-Dependent Collisional Cross-Section revelou-se desprezável, em conformidade com assumpções da literatura. Os efeitos dos processos de dissociação e de excitação vibracional revelaram-se mais acentuados para temperaturas a montante mais elevadas.

Palavras-chave: Reentrada, Hipersónico, Transporte, *State-to-state*

Abstract

This work studies nonequilibrium hypersonic flows surrouding space reentry vehicles. The design of such vehicles and its associated thermal protection systems relies on the accurate modelling of transport phenomena. In this thesis, dissociation and vibrational energy transfer relaxation processes are treated using a state-to-state kinetics approach. A numerical study is carried out to assess the impact of using state-specific transport coefficients in CFD simulations of hypersonic external flowfields. To this purpose, the Gupta-Yos/CCS macroscopic transport model, available in the SPARK code, has been transposed to state-to-state species, considering in a first approximation that state-specific transport properties are equivalent to the macroscopic ones. Additionally, a state-dependent collisional cross-section model has been implemented, taking into account the increase of collision cross-sections for vibrationally excited molecules. The code was successfully applied to the simulation of a 7 km/s nitrogen flow past a sphere. Different physical models were considered: Euler and Navier-Stokes state-to-state, Navier-Stokes one and two-temperature. Considering transport phenomena in a state-to-state approach resulted in smoother variations of the flow properties, with a 15% lower peak temperature and a similar shock position. Comparing the viscous state-to-state simulations with the two-temperature ones, the state-to-state approach yielded respectively a 10% and 5% larger shock standoff distance and peak temperature. A comparison of the standard state-to-state transport model with the one considering enchanced collision cross-sections yielded minimal differences in the obtained results, in agreement with the assumptions from the litterature. The effects of dissociation and vibrational excitation processes were confirmed to be emphasised for higher freestream temperatures.

Keywords: Reentry, Hypersonic, Transport, State-to-state

Contents

List of Tables

List of Figures

Nomenclature

Greek symbols

$[\tau]$	Viscous stress tensor.
β	Pre-exponential factor in Arrhenius equation.
Δ	Collision integral.
$\dot{\Omega}$	Thermal energy source term.
$\dot{\omega}$	Species source term.
μ	Viscosity coefficient.
ν	Stoichiometric coefficient on the product side of the chemical reaction.
ν'	Stoichiometric coefficient on the reactant side of the chemical reaction.
ν''	Stoichiometric coefficient.
$\overline{\Omega}$	Weighted average of cross-sections.
ϕ	Scale factor.
ρ	Density.
σ	Interaction distance.
τ	Characteristic relaxation time.
Θ	Macroscopic time.
θ_r	Temperature of reaction.
ε	Specific internal energy.

Roman symbols

$\vec{q}_c$	Conduction heat flux.
$\vec{q}_{rad}$	Radiative heat flux.
$\vec{u}$	Mean flow velocity.

A	Correlation constant in Arrhenius equation.
c	Mass fraction.
C_P	Specific heat at constant pressure.
C_V	Specific heat at constant volume.
D	Mass diffusion coefficient.
E	Total energy.
G	Gibb's free energy.
g	Degeneracy.
h	Enthalpy.
J	Mass diffusion flux.
K_b	Rate constant for the backward process of the chemical reaction.
k_B	Bolztmann constant.
K_f	Rate constant for the forward process of the chemical reaction.
K_{eq}	Equilibrium chemical constant.
Le	Lewis number.
M	Molar mass.
m	Mass.
N	Number of molecules.
n	Number density.
p	Pressure.
Q	Partition function.
R	Specific gas constant.
r	Internuclear distance.
Ru	Universal gas constant.
T	Temperature.
T_c	Controlling temperature.
V	Volume.
x	Molar fraction.

Subscripts

∞	Refers to upstream.
e	Refers to electrons.
exc	Refers to the electronic excitation energy mode.
h	heavy species.
int	Refers to internal energy mode.
k	k*th* energy mode.
m	Refers to molecules.
R	R*th* chemical reaction.
r	r*th* chemical species.
rot	Refers to rotional energy mode.
s	s*th* chemical species.
tra	Refers to translational energy mode.
v	v*th* vibrational energy level.
vib	Refers to vibrational energy mode.
VT	Vibration-translation energy transfer process.
w	w*th* vibrational energy level.

Superscripts

L	Losev.
MW	Millikan&White.
NS	Number of species.
o	Refers to formation.

Glossary

1T	One-temperature is an approach for modelling nonequilibrium flows, in which the assumption of thermal equilibrium is used.
2T	Two-temperature is an approach for modelling nonequilibrium flows, in which the assumption of thermal equilibrium between rotation and translation and between vibration and electronic excitation is used.
CCS	Collisional Cross-Section is the area around a particle in which the center of another particle must be in order for a collision to occur.
CFD	Computational Fluid Dynamics is a branch of fluid mechanics that uses numerical methods and algorithms to solve problems that involve fluid flows.
CLN	Constant Lewis Number is a widely used assumption in the modelling of mass diffusion.
FHO	Forced Harmonic Oscillator is a model that provides an analytic solution for the state-specific rates of energy transfer processes that involve vibrational levels.
FIRE	Flight Investigation of the Reentry Environment was a mission with the purpose of measuring radiative heat transfer at lunar return velocities.
FVM	Finite Volume Method is a method for representing and evaluating partial differential equations in the form of algebraic equations. Values are calculated at discrete places on a meshed geometry.

IPFN	Instituto de Plasmas e Fusão Nuclear is a research institute at Instituto Superior Técnico, Lisbon.
SM	Stefan-Maxwell is a set of equations that describes diffusion processes in multicomponent systems.
SPARK	Software Package for Aerodynamics Radiation and Kinetics is a CFD code developed and maintained at IPFN. It is a structured, finite volume code that solves the Navier-Stokes equations for a chemically reacting flow.
STS	State-to-State is an approach in the field of kinetics that regards the internal energy levels of chemical species as pseudo-species.
TPS	Thermal Protection System is the shield that protects the capsule against the intense heat fluxes experienced during reentry.

Chapter 1

Introduction

Space is the greatest untapped source of scientific knowledge from where endless possibilities arise. In the attempt to explore New Horizons, the development of novel and efficient Space technologies is of paramount importance. Up to now, a large majority of planetary exploration missions has been limited to one-way trips. Nevertheless, future sample return or manned missions will include a high-speed (superorbital) Earth entry return. Reentry vehicles will have to be capable of withstanding the severe aerothermodynamic environment caused by this specific class of atmospheric entry.

1.1 High-speed Atmospheric Entry

During entry into Earth's atmosphere, the vehicle gradually loses altitude and reaches denser regions of the atmosphere. Meanwhile, it must decelerate from speeds up to 13 km/s (the Stardust sample return capsule was the fastest man-made object to reenter Earth's atmosphere at 12.9 km/s [1]) to the subsonic regime. Considering that these velocities are much higher than the speed of sound, the internal energy of the flow is small when compared to its kinetic energy and the flow is said to be hypersonic [2]. This implies that strong shock waves will be formed: the changes in the flow properties occur abruptly and the flow thermodynamic processes are irreversible, causing a large increase in entropy. One of these processes is the conversion of a large amount of coherent translational energy (velocity) into agitation energy, which results in a significant increase in the translational temperature (up to 10^4-10^5 K). This energy will mostly be transported to the wake region of the flow, but a significant part will reach the spacecraft's surface, becoming necessary to estimate the corresponding convective and radiative fluxes. Moreover, under this high-temperature and low pressure conditions, the gas is in an extreme nonequilibrium state, enabling a series of fast and complex physicochemical processes (illustrated in Fig. 1.1), and ultimately reaches a new equilibrium condition (different from the upstream one) - see Fig. 1.2.

Typically, reentry capsules are designed as a blunt-body (as shown in Fig. 1.1) favouring shock detachment, in order to minimize the surface convective heat flux, at the expense of increasing radiative fluxes (Fig. 1.2). The detachment of the shock leaves room between the shock wave and the TPS (Ther-

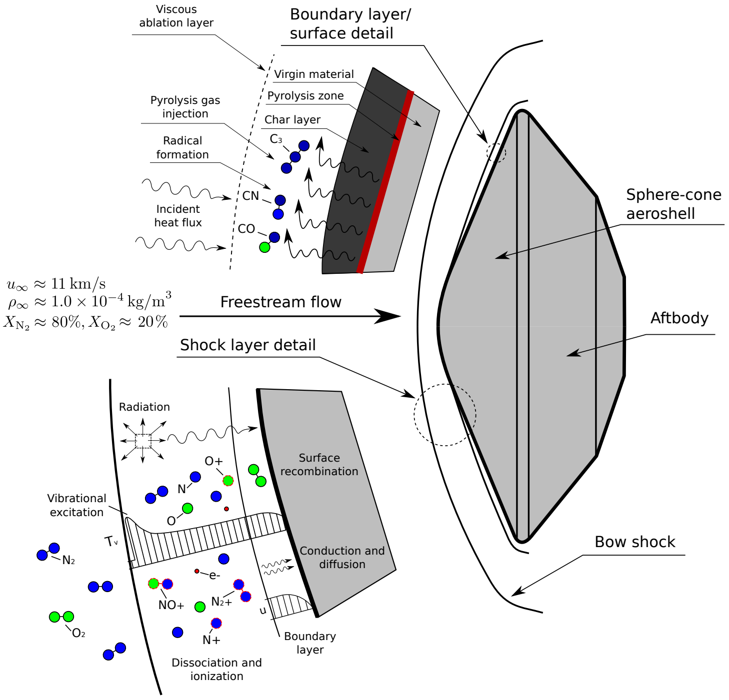

Figure 1.1: Illustration of the aerothermodynamic processes occurring in the shock layer and on the surface of a Stardust-type re-entry capsule at peak heating conditions [3].

mal Protection System) surface – the so-called shock layer - where endothermic relaxation, dissociation and ionization gradually cool down the gas, leading to smaller temperature gradients at the capsule's surface. These cooling phenomena prevent the complete depletion of the TPS and the destruction of the metallic airframe of the capsule (as in the case of the Space Shuttle Columbia accident in 2003, caused by localized TPS failure).

The endothermic relaxation processes occurring in the shock layer refer to the gradual excitation of the internal energy modes of the flow chemical species – electronic, vibrational and rotational modes - making it necessary to account for quantum chemical effects associated to interactions at microscopic scales [4, 5]. Collisional energy exchanges between the internal atomic and molecular degrees of freedom have to be properly simulated. The probability of molecular collisions depends on the corresponding cross-sections, which are defined as the area around a particle in which the center of another particle must be in order for a collision to occur. Hence, these cross-sections for energy transfer between different internal modes have to be accurately modelled, as they depend on the exchange process (for example, rotation-translation energy transfer is very efficient in a collision, whereas vibration-translation energy transfer is less efficient). The relaxation times for the different internal energy modes of an atomic/molecular species will accordingly be different [6]. Furthermore, as the shocked flow is highly energetic, dissociation and ionization processes are established downstream of the shockwave, after a small incubation time. Given that the time scales of internal modes relaxation and chemical reactions is long compared to the characteristic flow time, the flow is said to be both in thermal and chemical

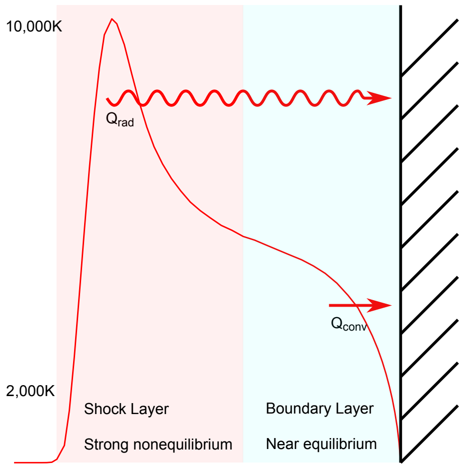

Figure 1.2: Illustration of the stagnation line temperature evolution: heat fluxes, shock and boundary layers regions.

nonequilibrium conditions [7, 8].

Thus, further developments in hypersonic flight technologies require a complete and detailed knowledge of the post-shock nonequilibrium phenomena. Ground-testing is not a fully viable option, considering that the reproduction of typical flow parameters, such as Mach and Knudsen numbers (the Knudsen number refers to the ratio of the molecular free path to the macroscopic length scale), is limited to certain ranges, making it impossible to precisely mimic a high-enthalpy reentry environment. Flight testing is mostly out of question, since it would be technically challenging and too expensive [9]. In response to these limiting factors, computational fluid dynamics (CFD) has been developed to become an effective approach and currently plays an important role in the design of planetary vehicles. CFD simulations use the Navier-Stokes equations to provide an accurate prediction of the hypersonic flowfield surrounding the vehicle at the most critical stages of the descent trajectory. Knowledge on flow properties such as heat flux, pressure, and shear stress, provides information on the thermal loads, aerodynamic forces and moments applied to the capsule, helping engineers optimize spacecraft shapes and flight control, select appropriate structures and materials, improve overall efficiency and, subsequently, reduce costs [9, 10].

The most advanced Navier-Stokes reentry simulations use macroscopic multi-temperature models to account for the nonequilibrium phenomena described above. These models assume that the populations of the internal energy modes of chemical species follow an equilibrium Boltzmann distribution at a characteristic temperature T_{int} (which is not necessarily the same as the flow temperature T). Although multi-temperature models are a powerful tool, for the extreme nonequilibrium conditions of a superorbital entry in excess of 10 km/s, there is strong departure from the Boltzmann distribution of the internal energy levels populations and these assumptions may not apply [11]. A more detailed and reliable strategy is the state-to-state approach, which treats each internal level as a separate species by solving the associated mass conservation equation, the so-called master equation. It quantifies the degree of nonequilibrium everywhere in the flow by determining the population densities in the quantum energy states of the internal energies [10]. However, the coupling of fluid dynamic equations with state-to-state kinetics translates into a computationally intensive system of partial differential equations and poses considerable challenges. Up to now, it has been implemented exclusively in Euler simulations [12], which do not provide any information on the effect of mass diffusion, viscosity and thermal conductivity.

The objective of this work is to implement state-specific transport models in a CFD code suited for space reentry simulations, thus, coupling Navier-Stokes fluid dynamic equations to the state-to-state kinetic theory. A long-term application of this study is the prediction of the radiative wall heat flux, which strongly depends on the results for the temperature of the shock layer provided by CFD simulations. For the sake of simplicity, ionization is neglected and only vibrational energy levels are considered.

1.2 State-of-the-art

Reentry flows were firstly studied by means of combining semi-empirical models and engineering correlations. Following this strategy, first estimates of the aerodynamic coefficients and heat fluxes on the forward body stagnation streamline can be obtained, yet it fails to provide insight into the complexity of the physicochemical phenomena occurring around the capsule. Furthermore, these techniques require oversimplistic assumptions that lead to great uncertainties and, consequently, to the need for very conservative safety factors when designing Thermal Protection Systems (TPS). In light of this, semi-empirical physical models started to be implemented in computational solvers, giving rise to CFD simulations. This approach has become a powerful tool towards reaching a deeper understanding of the gas dynamics processes that were pointed out in the previous section and, consequently, efficiently designing a reentry capsule. Given that CFD solutions are only as accurate as the underlying mathematical and physical models, it is necessary to verify and validate them by comparing the results against existing experimental ground-tests and flight data [3]. Notwithstanding the fact that flight experiments allow the exact replication of the encountered flow conditions, their focus is somewhat limited to macroscopic quantities (heat fluxes, forces, moments, etc.) and the extent to which microscopic processes affect the results is unknown [13]. In this section, a brief review of high-speed reentry ground experiments (Section 1.2.1) and computational studies (Section 1.2.2) is presented.

1.2.1 Ground Experiments

Hypervelocity reentry flows have been studied experimentally in shock tunnels for several decades now, through optical diagnostics. Being the simplest blunt-body designed shape, a forward body spherical geometry (spheres, hemisphere cylinders or blunted cones) has been widely used for parameter and model tests. Hornung [14] conducted a systematic experimental investigation on a reacting nitrogen flow over a spherical cylinder in a shock tunnel, in which he covered the maximum available range of relevant parameters. Particular focus was given to the influence of reaction rates and of the effect caused by free-stream nonequilibrium (which occurs when the stream is accelerated by nozzle expansion). In the T5 high-enthalpy facility at Caltech, Hornung and Wen [15] extended the previous work to the case of complex gas mixtures with several species and reactions, and the additional parameter of the dimensionless free-stream kinetic energy was taken into account. Further experimental investigations on hypersonic flows around blunted bodies have been conducted and later reviewed by Deiwert and Eitelberg [16], Holden [17], and Muylaert et al. [18]. It is important to note that the velocities achieved in the previous experiments never exceeded 8 km/s, recalling that it is never possible to fully replicate flight conditions to a satisfactory degree. Thus, ground-tests are used as indispensable tools to validate CFD codes, that remain the most economical and complete approach to study reentry environments, providing a detailed description of the corresponding physical phenomena.

1.2.2 Computational Modelling

The computational modelling of reentry hypersonic flows at low altitudes requires the numerical solution of an appropriate set of governing equations for the continuum flight regime: either the Euler equations or, preferably, the compressible Navier-Stokes equations, which account for the effect of mass diffusion, viscosity and thermal conductivity. In this section, a review of two different approaches for the modelling of nonequibrium (multi-temperature models and the state-to-state approach) as well as of high-temperature transport models is presented.

Multi-Temperature Approach

Accounting for thermochemical nonequilibrium is traditionally carried out through the use of multi-temperature models, with Park's two temperature model being the most widely used in Navier-Stokes solvers [9, 19–21]. This model assumes that the translational energy of the molecules is in equilibrium with the rotational one at a temperature T_{tra} and that the vibrational energy of the molecules is in equilibrium with the electron translational energy at a vibrational temperature T_{vib}. Scalabrin and Boyd [19] simulated an axisymmetric flow over the FIRE-II spacecraft under reentry conditions with the objective of calculating convective and radiative heating rates. Wilke/Blottner/Eucken [22] and Gupta-Yos [23] mixing rules are used as different transport models to determine the convective heat flux. The obtained results were in good agreement with total heat transfer flight measurements. Hao et al. [20] investigated the effect of two different 11-species chemical reaction models by simulating the reentry flow around the RAM-C II vehicle and the FIRE-II capsule configurations, using Wilke/Blottner/Eucken mixing rule to determine transport coefficients. A comparison between the effect of both transport models (Wilke/Blottner/Eucken and Gupta-Yos mixing rules) on four different flight conditions chosen from the trajectory of the Mars Pathfinder reentry vehicle is carried out in ref. [21]. The results provided by the approximate model (Wilke/Blottner/Eucken) were in good agreement with those determined by the collision integral model (Gupta-Yos), except for the chemical diffusion heat fluxes, which were significantly larger in the first case, particularly in the stagnation point region.

State-to-State Approach

Considering a more general state-to-state approach, which does not require imposing a Boltzmann distribution for the internal levels of chemical species, it was shown that highly non-Boltzmann vibrational distributions are indeed found in the stagnation region of a nitrogen flow past a blunt-body [24]. Likewise, Josyula and Bailey [25] ascertain the need to take into account dissociation processes at the quantum level when modeling vibration-dissociation coupling. It becomes apparent that representing the nonequilibrium vibrational and chemical kinetics in terms of master equations that account for cross-sections in the chemical reactions and vibrational transition probabilities is indispensable when strong deviations from Boltzmann distributions are present. However, this so-called state-to-state approach suffers from drawbacks such as high computational cost and lack of data on rate coefficients and internal energy transitions, among others [26].

It was only in recent years that the state-to-state kinetic theory started to be employed in computing codes for gas flows. Initially, inviscid flows behind shock waves [27–29], in nozzles [30, 31] and along the stagnation line [32] were studied. With the development of advanced numerical methods and new data sets for the collisional cross-sections, the coupling of state-to-state kinetics to fluid dynamics was extended to two-dimensional Euler simulations. Josyula et al. [6, 8] simulated a steady-state, hypersonic blunt-body nitrogen flow at 7 km/s around a hemisphere cylinder, with the objective of predicting nonequilibrium behavior in reentry flows. Lopez et al. [33] solved the master equations, coupled to the momentum and the energy conservation equations, for the two-dimensional axisymmetric inviscid case to simulate high-temperature typical reentry conditions. The vibrational state-specific model was then compared with the multitemperature approach. It was observed that the vibrational state-specific model prevents the non-physical vibrational temperature overshoot phenomenon, a well-known drawback of multi-temperature models, and that the state-resolved description of the vibrational levels does not influence the predicted shock standoff distance. Bonelli et al. [10] succeeded in reducing computational costs by exploring the power of GPUs. A high-enthalpy reentry flow around a sphere was simulated and results provided by using detailed state-to-state air kinetics and multi-temperature models were compared. It was shown that state-to-state outcomes are in better agreement with experimental findings than those provided by multi-temperature models.

Despite the relevance of the state-to-state approach in studying inviscid flows, taking diffusion processes into account is of paramount importance when predicting the properties of gas flows and providing accurate estimations of the convective heat fluxes. Very few Navier-Stokes reentry simulations have accounted for the state-specific quantum distributions, all of them performed by Josyula. In ref. [34], vibrational energy distributions are modeled by the master equation and a chemical-vibrational source term is included in the mass conservation equation. A “hybrid” model is developed, in which this source term is updated according to the results of the state-specific master equation, after each Navier-Stokes iteration. Ref. [35] evaluates the influence of state-to-state kinetics on the prediction of transport properties and wall heat fluxes, using three different methods for calculating transport coefficients: simplified methods of Blottner curve fits, Variable Hard-Sphere model and the more detailed state kinetic models. The consideration of diffusive fluxes if achieved by means of post-processing. Results provided by a Mach 23 air flow reentry simulation showed that the Variable Hard-Sphere model leads to reduced shock thickness and slightly thicker boundary layer. This work is further developed in refs. [36, 37].

High-Temperature Transport Models

The Boltzmann equation provides the most detailed description of gas flows by means of describing the behavior of the gas at the microscopic scale. It is used do derive the macroscopic fluid dynamic conservation laws for mass, momentum and energy using the Chapman-Enskog method, which relies on the asymptotic expansion of the Boltzmann equation in the Knudsen number. The zero order approximation of this method yields the Euler equations. First order corrections to this approximation yield the Navier-Stokes equations, providing accurate formulas for the mixture transport properties (mass diffusion, viscosity and thermal conductivity) which relate them to microscopic interaction, expressing their dependence on the gas mixture composition as well as on the populations of the internal energy levels [38]. If a multi-species gas mixture is considered, which is the case of this work, a mixture viscosity μ and a mixture thermal conductivity λ transport coefficients are defined for the momentum conservation equation and for the energy conservation equation, respectively. Furthermore, since one mass conservation equation is defined for each species s, a mass diffusion transport coefficient D_s must be determined for each species.

- **Macroscopic Transport Models**

In the multi-temperature approach, transport models are derived on the basis of equilibrium Boltzmann distributions of the molecules over the energy states. Hence, these models provide expressions for the transport coefficients of chemical species [39]. In this work, the Wilke/Blottner/Eucken and the Gupta-Yos/CCS (Collision Cross-Section) models are used. The Wilke/ Blottner/Eucken model is a mixing rule which assumes that all interactions between any particles present the same cross-section. The Gupta-Yos/CCS model, on the other hand, is a more detailed mixing rule, which accounts for the different cross-sections corresponding to each collision.

In refs. [40–45], the effect of these and other transport models on the predicted flowfield properties of planetary entry vehicles is investigated within the framework of multi-temperature models. Palmer [41] compares three different mixing rules for computing the viscosity of neutral and ionized species: Wilke, Gupta-Yos and Armaly-Sutton [46]. The author concludes that Wilke's mixing rule is the least accurate method, whereas the Gupta-Yos mixing rule not only provides acceptable results for weakly or nonionized flows but is computationally faster as well. The Armaly-Sutton mixing rule, in turn, is applicable to higher temperatures and strongly ionized flows, yet more computationally expensive than Gupta-Yos model. Gosse and Candler [44] compared the CLM (constant Lewis number) Fickian diffusion method [47] against two multicomponent models, the SCEBD (Self-Consistent Effective Binary Diffusion [48, 49]) and the SM (Stefan-Maxwell Iterative method [50]) methods. The SCEBD and SM methods showed good agreement between each other, predicting lower heating values than the CLN method, especially when the flow became completely dissociated. Using four different trajectory points of the Stardust sample return capsule as a test case, Alkandry et al. [45] evaluated the effect of the following different methods: Wilke's mixing rule with species viscosities calculated using Blottner's curve fits and species thermal conductivities determined with Eucken's relation; Gupta-Yos mixing rule with collision cross-section (CCS) data. It was observed that the heat transfer predicted using the Wilke/Blottner/Eucken model is in good agreement with the Gupta-Yos/CCS solution only for relatively slow Earth entry speeds. For higher altitudes, the Wilke/Blottner/Eucken model overpredicted the surface heat flux by up to 60% comparing to the Gupta/CCS model .

- **State-Specific Transport Models**

The state-to-state approach accounts for deviations of level populations from the equilibrium Boltzmann distribution. Hence, in the coupling of the latter to fluid dynamic equations, the macroscopic conservation equations for mass, momentum and total energy are considered together with the equations for level populations of different chemical species [39]. Formulas for the state-specific transport coefficients were obtained by Nagnibeda and Kustova [51], on the basis of the state-to-state kinetic theory approach.

Within this framework, one-dimensional studies were conducted. Bruno et al. [52] have shown that state-to-state vibrational kinetics significantly impacts the transport coefficients under strong nonequilibrium conditions. In fact, transport coefficients determined by realistic vibrational distributions can be up to an order of magnitude greater than those obtained by considering Boltzmann distributions at a specific vibrational temperature. Kustova et al. [39, 53, 54] investigated the influence of vibrational and chemical kinetics on heat transfer and diffusion in hypersonic flows. It is observed that the fluid dynamic variables and heat fluxes obtained considering state-specific or equilibrium Boltzmann distributions are substantially different. Furthermore, Armenise [55–57] has done considerable work in describing the boundary layer surrounding a body under reentry conditions, on the basis of the kinetic theory of gases. From a more theoretical perspective, state-to-state studies on vibrational distributions led to some noteworthy results. Kustova and Kremer [58] demonstrated that the size of vibrationally excited molecules strongly depends on the vibrational level. Yet the estimated coupled effect of molecular size and non-Boltzmann distributions on the transport properties of the flow is negligible [52, 59].

These past studies helped setting a framework for full vibrationally-specific 2D simulations of hypersonic flows, mostly focusing on providing a better modeling/understanding of nonequilibrium chemical kinetic processes. Upon these foundations, a significant task that remains is the inclusion of a full state-specific transport model in the governing fluid dynamic equations. This work aims at providing the first groundwork for this task.

1.3 Objectives

The primary aim of this thesis is to assess the influence of state-specific transport coefficients in the prediction of reentry flow properties and corresponding convective heating. The specific aims of this thesis are therefore to:

- Adapt the theoretical formulation of Wilke/Blottner/Eucken and Gupta-Yos/CCS transport models to state-specific species.
- Formulate the State-Dependent Collisional Cross-Section transport model, which accounts for the enhanced cross-sections of vibrationally excited molecules.
- Implement the previously mentioned transport models in the code SPARK.
- Simulate a full state-to-state Navier-Stokes nitrogen reentry flow using two different transport models: Gupta-Yos/CCS model adapted to state-specific species and State-Dependent Collisional Cross-Section model (Wilke/Blottner/Eucken model adapted to state-specific species is used only for convergence purposes).
- Compare the obtained results to the following cases: Euler state-to-state; Navier-Stokes one-temperature with Gupta-Yos/CCS transport model; Navier-Stokes two-temperature with Gupta-Yos/CCS transport model.

In order to accomplish these objectives, the hypersonic CFD code SPARK - Simulation Platform for Aerodynamics, Radiation and Kinetics - maintained by IPFN (Instituto de Plasmas e Fusão Nuclear) will be used.

1.4 Thesis Outline

This work is divided into five main chapters, the content of which is specified as follows:

- Chapter 1- the present chapter comprises an introduction to High-speed reentry physics, State-of-the-art, Objectives of the master thesis and corresponding Outline.
- Chapter 2 presents the set of governing equations, as well as the physical models used to formulate the problem.
- Chapter 3 explains the numerical implementation. It gives an overview of the code's structure and numerical methods, describes the definition of consistent databases and presents the numerical setup of the simulations to be performed.
- Chapter 4 shows and discusses numerical results.
- Finally, Chapter 5 presents the conclusions and future work.

Chapter 2

Governing Equations and Physical Models

In this chapter, the governing equations for hypersonic reentry flows are presented and discussed. As introduced in Section 1.1 of Chapter 1, studying the aerothermodynamic environment surrounding a reentry vehicle implies accounting for different complex physical processes by means of appropriate modelling. These may be split in five specific disciplines:

- Fluid governing equations (Section 2.1)
- Thermodynamic models (Section 2.2)
- Chemical kinetics models (Section 2.3)
- Energy exchange models (Section 2.4)
- Transport models (Section 2.5)

In this work, the implementation of the models listed above follows a state-specific formulation, which allows a more accurate description of flows under such extreme nonequilibrium conditions. There are key conceptual differences between a macroscopic hydrodynamic model (which is the case of multi-temperature models), where the degrees of freedom (translational and internal) of the chemical species are treated globally, and a state-to-state model, where each internal energy level is treated as pseudo-species[1]. In the former case of macroscopic nonequilibrium models, additional conservation equations for the internal modes have to be added. These do not exist when state-to-state models are concerned. Instead, energy exchanges between the translational and internal modes are implicitly accounted for in the production and destruction of pseudo-species in the different degrees of internal excitation, i. e. different energy states, resorting to so-called state-to-state kinetic models.

Whenever applicable, each section of this chapter will discuss in detail the differences between both macroscopic and state-to-state descriptions

---

[1] note that even with state-to-state modelling, the translational degree of freedom is treated globally with a characteristic temperature T_{tra}, otherwise the Navier-Stokes equations don't apply and Direct Simulation Monte Carlo models have to be considered.

2.1 Fluid Governing Equations

Conditions of a continuum flow regime are considered throughout this work. Accordingly, the most suited set of governing equations are the Navier-Stokes conservation equations for hypersonic flows, presented below. In the case of a multicomponent flow, there are as many mass conservation equations as species (whether macroscopic chemical species or state-to-state pseudo-species). The mass conservation equation 2.1a for each species s account for the production and destruction source terms $\dot{\omega}_s$ – based on the local state of the flow and the characteristic time scale defined for each reaction – and for the mass diffusion terms. The momentum equation 2.1b enforces Newton's Second Law. The total energy equation 2.1c enforces the conservation of energy.

$$\frac{\partial(\rho c_s)}{\partial t} + \vec{\nabla}.(\rho c_s \vec{u}) = \vec{\nabla}.\vec{J_s} + \dot{\omega}_s \tag{2.1a}$$

$$\frac{\partial(\rho \vec{u})}{\partial t} + \vec{\nabla}.(\rho \vec{u} \otimes \vec{u}) = \vec{\nabla}.[\tau] - \vec{\nabla} p \tag{2.1b}$$

$$\frac{\partial(\rho E)}{\partial t} + \vec{\nabla}.(\rho E \vec{u}) = \vec{\nabla}.\Big(\sum_k \vec{q}_{c_k} + \sum_s \vec{J_s} h_s + \vec{u}.[\tau] - p\vec{u}\Big) \tag{2.1c}$$

In Eqs. 2.1a-2.1c, ρ is the density, $\vec{u}$ the mean velocity in vectorial form, c_s the chemical species s mass fraction, $\vec{J_s}$ the chemical species s mass diffusion flux, $\dot{\omega}_s$ the chemical species s source term, $[\tau]$ the viscous stress tensor, p the pressure, E the total energy, $q_{\vec{c_k}}$ the conduction heat flux of the kth thermal energy mode and h_s the enthalpy of the chemical species s.

As aforementioned, in the case of a thermal nonequibrium macroscopic description, an additional conservation equation for the internal modes energy has to be accounted for (Eq. 2.1d). This enforces the conservation of energy for each thermal energy mode:

$$\frac{\partial(\rho \epsilon_k)}{\partial t} + \vec{\nabla}.(\rho \vec{u} h_k) = \vec{\nabla}.\Big(\vec{q}_{c_k} + \sum_s \vec{J_s} h_{s,k} + \vec{q}_{rad}\Big) + \dot{\Omega}_k \tag{2.1d}$$

where $q_{\vec{rad}}$ is the radiative heat flux, ε_k is the global thermal energy of the kth thermal energy mode and $\dot{\Omega}_k$ the thermal energy source term.

In this work, radiation is not considered, thus $q_{\vec{rad}} = 0$. The remaining terms are defined according to the theoretical models presented in subsequent sections.

2.2 Thermodynamic Models

A chemically reacting flow must be described by a multi-component gas model, which is characterized as a mixture of individual chemical species into a single phase. This means that the macroscopic properties of the flow (density, temperature, viscosity, etc.) are defined as function of the local composition of the gas, which, in turn, can be described by classical chemical thermodynamics. In fact, thermodynamics and chemistry serve as a basis for the study of high-temperature gas dynamics and the understanding of equilibrium and nonequilibrium conditions of the flow. In this regard, general definitions and basic thermodynamic relations used to calculate the chemical composition of an equilibrium chemically reacting mixture can be found in Appendix A.1. In this work, a multi-component N_2/N mixture is used to model the Earth's atmosphere in a simplified manner, in order to avoid excessive computational cost.

2.2.1 Quantization of the Internal Degrees of Freedom

Besides the chemical composition that defines a given state of a reacting mixture, the classical thermodynamic theory provides relations between the various thermodynamic properties of the gas, keeping in mind that a thermodynamic state is completely defined by two thermodynamic state variables. However, in order to explicitly calculate the values of the thermodynamic properties (internal energy, enthalpy, entropy, etc.) it is necessary to fall back on the microscopic description of the gas, in which statistical thermodynamics plays a major role. In subsequent sections, it will become clear how this approach is crucial in the analysis of nonequibrium high-temperature flows.

At the microscopic level, it is assumed that the gas consists of a large number of individual molecules, each one having different modes of energy or internal degrees of freedom. As illustrated in Fig. 2.1, these degrees of freedom can be categorized into four thermal energy modes. Since a N_2/N mixture is used throughout this work, we only refer to diatomic molecules or atoms.

(a) Translational Mode (b) Rotation Mode

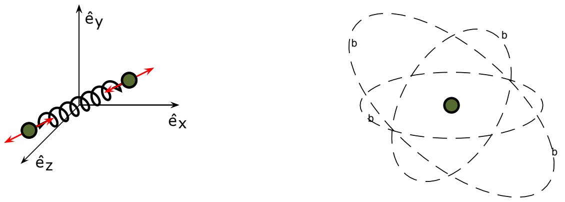

(c) Vibration Mode (d) Electronic Excitation Mode

Figure 2.1: Energy modes. [60].

As a molecule moves through space, its center of mass acts as a source of translational kinetic energy. The motion of the molecule can be resolved into three components (x, y, z), each one contributing to the total kinetic energy. Thus, it is said to have three translational thermal degrees of freedom. Similarly, a molecule rotates about the three orthogonal axes in space. The energy associated to this rotational velocity and to the molecule's moment of inertia contributes to the total rotational kinetic energy in the three different ways, associated to each one of the axes. Given that the moment of inertia about the internuclear axis (z axis in the figure) is negligible, it is said to have only two rotational thermal degrees of freedom. Furthermore, the atoms of a diatomic molecule vibrate with respect to an equilibrium position within the molecule. This vibrational motion adds one or more degrees of freedom depending on whether the molecule is diatomic or polyatomic. Finally, the orbital motion of electrons about atoms or molecules adds yet another energy storage mode. Given that electronic motion is generally complex, the concept of thermal degrees of freedom does not strictly apply in this case.

Accordingly, the total energy of a chemical species ε_s is defined by the sum of these contributions:

$$\varepsilon_s = \varepsilon_{tra,s} + \varepsilon_{rot,s} + \varepsilon_{vib,s} + \varepsilon_{exc,s} \tag{2.2}$$

For an atom, only translational and electronic energies are considered:

$$\varepsilon_s = \varepsilon_{tra,s} + \varepsilon_{exc,s} \tag{2.3}$$

Since the microscopic motion of atoms and molecules is governed by quantum mechanic equations, the internal energy levels, instead of taking values in a continuous range, can only take certain discrete values. For this reason, these energies are said to be quantized, as represented in the ladder-type diagram shown in Fig. 2.2.

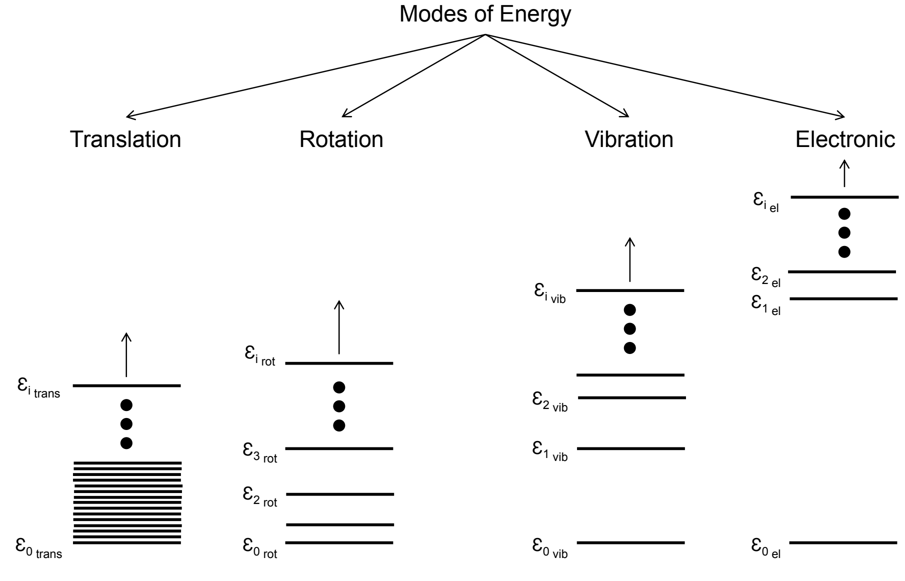

Figure 2.2: Diagram for the energy levels of the different thermal modes [61]

A single-species (denoted by s) system is therefore composed of a grand total of N_s molecules, which is the sum of the species fractions $N_{j,s}$ that occupy a given energy level $\varepsilon_{j,s}$. We have:

$$N_s = \sum_j N_{j,s} \tag{2.4}$$

$N_{j,s}$ is defined as the population of the energy level $\varepsilon_{j,s}$ and the set of numbers formed by the several values of $N_{j,s}$ for each energy level is defined as the ***population distribution***. Another name for the population distribution, meaning a given set of $N_{j,s}$, is a ***macrostate***. Over time, molecular collisions occur inside a system and, at any given instant, the population distribution can change, as the molecules depart from one energy level to another.

Molecular orientation is also quantized. Consequently, for a given energy level ε_j, different orientations are possible and different states will exist within that energy level. The number of states in the same energy level is called the ***degeneracy***, denoted by g_j. The way molecules are distributed in different states within each energy level, at a given instant in time, is called the ***microstate***.

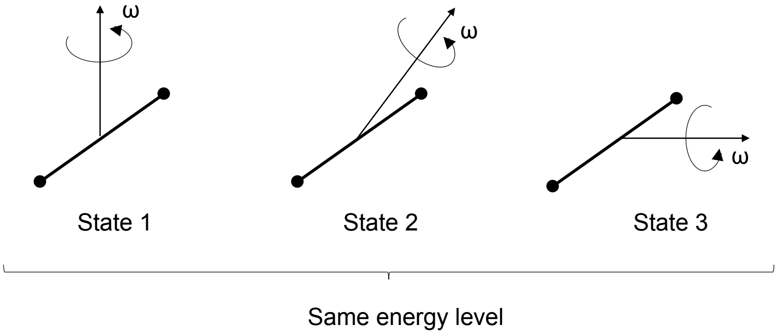

Figure 2.3: Illustration of different energy states according to molecular orientation, within the same energy level [61].

When a Boltzmann distribution for the internal levels is achieved with a characteristic temperature T for a given chemical species s, the population of these levels may simply be expressed according to the partition function Q_s:

$$\frac{N_{j,s}}{N_s} = \frac{g_{j,s} \exp\Big(- \frac{\varepsilon_{j,s}}{k_B T}\Big)}{Q_s} \tag{2.5}$$

A partition function translates a sum over the allowed energy states of the system, with each state weighted by a statistical factor. It is only function of the system volume V and temperature T:

$$Q_s = \sum_j g_{j,s} \exp\Big(- \frac{\varepsilon_{j,s}}{k_B T}\Big) = f(T,V) \tag{2.6}$$

where k_B denotes the Boltzmann constant.

The mathematical formulation used to determine the thermodynamic properties (internal energy and enthalpy) of a multi-component mixture is presented in Appendix A.2 in more detail.

2.2.2 Thermodynamic Nonequilibrium

Thermodynamic nonequilibrium may occur in a gas at different levels. As a matter of fact, full thermodynamic equilibrium is achieved in very few places in the universe, and most notably in the inside of stars, where the chemical composition and the internal levels populations of the gas are homogeneous, at a characteristic temperature T, and photons in the gas follow a Plank blackbody distribution at the same characteristic temperature. In room air, all the equilibrium conditions are fulfilled, except for radiative equilibrium, which is not achieved.

As a rule of thumb, as the temperature of a gas increases and the density/pressure decrease, the more prone it will be to departure from equilibrium, firstly chemically, then thermally, and ultimately Boltzmann nonequilibrium is reached. Higher temperatures lead to a more energetic gas, favouring the population of higher energy states or the creation of higher energy species and ions. Lower densities/pressures, on the other hand, translate into less molecular collisions that effectively redistribute the energy throughout the gas and, consequently, higher energy states tend to remain populated.

It is therefore obvious that thermodynamic nonequilibrium plays a central role in atmospheric entry flows due to its high postshock temperatures and low to moderate postshock pressures (up to a few bars). Here we will briefly outline departure from equilibrium at different levels, except for departure from radiative equilibrium, which is out of the scope of this work.

Chemical and Ionization nonequilibrium

When the chemical composition of a gas is invariant in space and time, the gas is said to be in chemical equilibrium. Thermodynamically speaking this occurs when the Gibbs free energy of the gas is minimized, and this may be found accounting for the partition functions of the flow species. The minimization of the Gibbs free energy translates into:

$$\sum_s G_s \mathrm{d}n_s = 0 \tag{2.7}$$

where G_s and n_s are, respectively, the Gibbs free energy of chemical species s per mole of s and the number of moles of s.

While chemical equilibrium is not achieved in full in a gas, it may still be in ionization equilibrium. On the contrary, a gas in chemical equilibrium is necessarily in ionization equilibrium. The populations of the electrons N_e, ions N_i and neutrals N_h are governed by the Saha equation:

$$N_e \left(\frac{N_i}{N_h}\right) = \frac{2Q_i}{Q_h} \left(\frac{2\pi m_e k_B T_e}{h^2}\right)^{3/2} \exp\left(-\frac{E_i - \Delta E_i}{k_B T_e}\right) \tag{2.8}$$

This equation remaining valid even in the case of thermal nonequilibrium between the electrons and heavy species ($T_e \neq T_h$)[2]. Details on ionization processes will not be covered further, since it is out of the scope of this work.

In a nonequilibrium situation, the chemical composition of a gas may only be described with a chemical kinetic model (this will be discussed in detail in Section 2.3) and transport properties for each individual species need to be considered (Section 2.5).

---

[2] even though this is disputed by some authors

Thermal nonequilibrium

Thermal nonequilibrium occurs when the internal populations for each atomic and molecular degrees of freedom follow a Boltzmann distribution with different characteristic temperatures each mode:

$$T_{tra} \neq T_{rot} \neq T_{vib} \neq T_{exc} \neq T_{el} \tag{2.9}$$

In this case, the conservation equations for each internal mode have to be considered (Eq. 2.1d), as well as corresponding energy exchange terms. These will be discussed (for the specific case of this work) in Section 2.4.

As a consequence of the different energy spacings for each mode (see Fig. 2.2) we have the following hierarchy for the respective equilibration times:

$$\tau_{tr} < \tau_{rot} \ll \tau_{vib} \ll \tau_{exc} \sim \tau_{el} \tag{2.10}$$

This is not always the case for higher temperatures, where increasing energy spacings for rotation, and decreasing spacings for vibration may lead to an inversion of the equilibration times [62, 63].

In thermal nonequilibrium, thermal conductivity of individual modes (for each species) needs to be considered, at the relevant characteristic temperatures.

Boltzmann nonequilibrium

If one or more internal modes fail to achieve a Boltzmann distribution, then so-called ”State-to-State” models have to be considered. In this specific case, each level is considered as a pseudo-species, and one mass conservation equation need to be considered for each one. Consequently, detailed state-specific kinetic models must be developed (discussed in Section 2.3.1), and individual transport properties have to be devised for each internal state (see Section 2.5).

2.3 Chemical Kinetic Models

In the equation for mass conservation of each species s (Eq. 2.1a), the kinetic source term $\dot{\omega}_s$ concerns the mass production/destruction rate of each species s and is determined by a chemical-kinetic model. It depends on the reversible chemical reactions occuring in the flow and the respective chemical rates. A generic elementary reaction R (a reaction that takes place in a single step) is defined as follows:

$$\sum_{s=1}^{NS} \nu'_s x_s \underset{K_b}{\overset{K_f}{\rightleftharpoons}} \sum_{s=1}^{NS} \nu''_s x_s \tag{2.11}$$

where x_s is the molar fraction of species s, ν'_s is the stoichiometric coefficient for reactant s, ν''_s is the stoichiometric coefficient for product s, K_f is the forward rate constant and K_b is the backward rate constant.

K_f and K_b are not independent, instead they are related through the so-called detailed balance principle through the equilibrium constant K_{eq}:

$$\frac{K_f}{K_b} = K_{eq} \tag{2.12}$$

where K_{eq} is related to the equilibrium chemical concentrations and may be determined from the reactant and product species partition functions, both in the conditions of thermal equilibrium and nonequilibrium [64].

The forward rate constants are usually measured experimentally for a given temperature range and fitted to an Arrhenius equation:

$$K_f = AT^{-\beta} \exp\left(-\frac{\theta_r}{T} \right) \tag{2.13}$$

where A, β and θ_r are respectively a constant, the pre-exponential factor and the temperature of reaction.

The kinetic source term $\dot{\omega}_s$ is then defined as:

$$\dot{\omega}_s = M_s \sum_R (\nu''_{sr} - \nu'_{sr}) \left[K_{f_R} \prod_s x_s^{\nu'_{sr}} - K_{b_R} \prod_s x_s^{\nu''_{sr}} \right] \tag{2.14}$$

where M_s is the molar mass of species s and the index r stands for a given reaction.

2.3.1 State-to-State Kinetics

As previously discussed, state-specific models treat each internal level as a pseudo-species, allowing the determination of more accurate non-Boltzmann distributions for entry flows. Nevertheless, as this is not yet a fully established discipline, there is not a rigorous and detailed model capable of treating all the internal states of the air species (such as described in Fig. 2.2). The reasons for this are: 1) The number of internal states in a high-temperature gas such as Air is too extensive for the current-day computational capabilities; 2) The quantum models for treating collisional excitation of molecular internal states still lack refinement, and more importantly, generalized experimental validation [65].

Currently, most studies using state-specific models are focused on molecular vibrational excitation and dissociation. The main reason is that this is a relatively tractable problem (with diatomic molecules typically having around 40 to 60 vibrational levels), but also because molecular vibrational excitation and dissociation are key physical processes that occur behind a shockwave, favouring further chemical reactions that ultimately lead to the formation of an atmospheric entry plasma. Among other more detailed (yet computationally intensive) models, the Forced Harmonic Oscillator (FHO) theory has been utilized quite successfully, yielding physically consistent vibrational state-specific rates K_f and K_b that accurately reproduce thermal dissociation rates in the Boltzmann equilibrium limit.

This semiclassical model considers the excitation of an harmonic oscillator by another body as it approaches and moves away from the oscillator, allowing the determination of the probabilities of transition from one vibrational level to another. This theory is strictly valid in a 1D configuration, but it can be generalized to a 3D geometry.

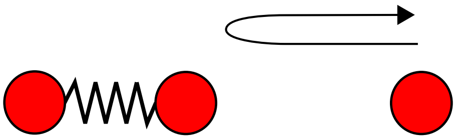

Figure 2.4: Forced Harmonic Oscillator Model

The FHO theory allows to determine multiquantum, vibrationally state-specific rates, as function of transition probabilities, for kinetic mechanims of the following types:

- Vibration-Translation (V-T)

$$\text{AB(v)+M} \rightarrow \text{AB(v} + \Delta\text{v)+M} \tag{2.15}$$

- Vibration-Vibration-Translation (V-V-T)

$$\text{AB(v)+AB(w)} \rightarrow \text{AB(v} + \Delta\text{v)} + \text{AB(w} + \Delta\text{w)} \tag{2.16}$$

- Vibration-Dissociation (V-D)

$$\text{AB(v)+M} \rightarrow \text{A + B + M} \tag{2.17}$$

where v and w denote different vibrational levels. The complex mathematical formulation of the FHO theory, including equations that provide transition probabilities for each process type, can be found in Ref. [66].

2.4 Energy Exchange Models

As explained before, in thermal nonequilibrium with Boltzmann distributions, Eq. 2.1d must be considered. In this equation, $\dot{\Omega}_k$ is defined as the thermal energy source term. In the two-temperature model (which assumes that $T_{tra} = T_{rot}$ and $T_{vib} = T_{exc}$), this term concerns the translational to vibrational energy transfer processes. The translational to vibrational energy transfer rate per unit volume of molecular species s is given by the Landau-Teller equation:

$$\dot{\Omega}_{V-T,s} = \rho_s \frac{\varepsilon^{eq}_{vib,s}(T_{tra}) - \varepsilon_{vib,s}(T_{vib})}{\tau_{VT,s}} \tag{2.18}$$

where ρ_s is the mass density of species s, $\varepsilon^{eq}_{vib,s}$ is the vibrational energy per unit mass of species s at equilibrium, $\varepsilon_{vib,s}$ is the vibrational energy per unit mass of species s and $\tau_{VT,s}$ is the vibrational relaxation time of species s.

The analytic expression for the vibrational energy per unit mass of each chemical species $\varepsilon_{vib,s}$ is obtained using a Treanor distribution (equivalent to a Boltzmann distribution for the low-lying vibrational levels) over the vibrational levels, yielding:

$$\varepsilon_{vib,s} = R_s \frac{\theta_{vib,s}}{\exp\left(\dfrac{\theta_{vib,s}}{T}\right) - 1} \tag{2.19}$$

where R_s is the specific gas constant and $\theta_{vib,s}$ is the characteristic vibrational temperature of chemical species s.

The vibrational relaxation time of each species $\tau_{VT,s}$ depends on the vibrational relaxation times of the interactions with collision partners r and the corresponding molar fractions x_r, as follows:

$$\tau_{VT,s} = \left(\sum_{r=1}^{NS} x_r\right) \cdot \left(\sum_{r=1}^{NS} \frac{x_r}{\tau_{s,r}}\right)^{-1} \tag{2.20}$$

The vibrational relaxation times associated with each interaction (s, r) can be defined according to the Millikan&White model [67], with Park's correction:

$$\tau_{s,r}^{MW} = \exp\left(A_{s,r}^{MW}\left(T^{-\frac{1}{3}} - B_{s,r}^{MW}\right) - 18.42\right)\left(\frac{p}{101325}\right)^{-1} + \left(N_s\sigma_s\left(\frac{8RuT}{\pi M_s}\right)^{\frac{1}{2}}\right)^{-1} [s] \tag{2.21}$$

where T and p are the gas temperature and pressure, respectively, N is the number density, σ is the effective vibrational cross-section, R_u the universal gas constant and M the molar mass. This model has been traditionally utilized for air species.

Alternatively one may resort to the Losev model [68], valid for temperatures ranging between 300 to 40000K:

$$\tau_{s,r}^{L} = \exp\left(A_{s,r}^{L} + B_{s,r}^{L}T^{-\frac{1}{3}} + C_{s,r}^{L}T^{-\frac{2}{3}} + D_{s,r}^{L}T^{\frac{1}{3}}\right)\left(\frac{p}{101325}\right)^{-1} [s] \tag{2.22}$$

which has been developed for treating vibrational relaxation on Venus and Mars (CO_2/N_2) entry flows.

2.5 Transport

In high-temperature flows, an accurate estimation of the flow properties, specifically convective fluxes, is extremely reliant on the accurate determination of multicomponent viscosity, mass and energy diffusion processes. Mass diffusion occurs because of random molecular motion and concentration gradients and is defined as the mass transport through molecular exchange. Self-diffusion concerns with transport of molecules due to the interaction with identical molecules. Viscosity is also associated to molecular interactions and establishes the relation between applied stress and strain rate. Thermal conductivity is related to the transport of random molecular translational and internal energy, which can be translated into the mean thermal energy of the flow [69].

In the conservation equations previously stated (Eqs. 2.1a - 2.1c), the diffusion processes are represented by the following quantities: $\vec{J}_s$, $[\tau]$ and $\vec{q}_{c_k}$. These quantities define the dissipative fluxes and are usually a function of their respective transport coefficient and gradient. Table 3.1 lists all the dissipative fluxes and their respective transport coefficient and gradient.

Table 2.1: Dissipative fluxes and corresponding transport coefficients and gradients. Presented in S.I. units

	Dissipative Flux		Transport Coefficient		Gradient	
Mass Diffusion	$\vec{J}_s$	kg.m^{-2}.s^{-1}	D_s	m^2.s^{-1}	$\vec{\nabla}(c_s)$	m^{-1}
Viscosity	$[\tau]$	N.m^{-2}	μ	kg.m^{-1}.s^{-1}	$\vec{\nabla}(\vec{u})$	s^{-1}
Thermal Conductivity	$\vec{q}_{c_k}$	J.m^{-2}.s^{-1}	λ_k	J.m^{-1}.s^{-1}.K^{-1}	$\vec{\nabla}(T_k)$	K.m^{-1}

The mass diffusion flux $\vec{J}_j$ is as described by Fick's Law of diffusion:

$$\vec{J}_s = \rho D_s \vec{\nabla}(c_s) \tag{2.23}$$

where D_s represents the sth species mass diffusion coefficient.

The viscous stress tensor $[\tau]$ assumes a Newtonian fluid and the Stokes hypothesis for the normal stresses:

$$[\tau] = \mu\Big(\vec{\nabla}\vec{u} + (\vec{\nabla}\vec{u})^T\Big) - \frac{3}{2}\mu\Big(\vec{\nabla}.\vec{u}\Big)[I] \tag{2.24}$$

where μ is the viscosity coefficient.

The conduction heat flux for each thermal energy mode, $\vec{q}_{c_k}$, is assumed to be given by Fourier's Law of heat conduction:

$$\vec{q}_{c_k} = \lambda_k \vec{\nabla}(T_k) \tag{2.25}$$

As discussed in the state-of-the art (Section 1.2), a detailed state-specific model has been recently proposed by Nagnibeda and Kustova [51]. A full implementation of this model is desirable on the long run. For now this work considers a simple transposition of the macroscopic transport properties to the state-to-state approach by adapting the Wilke/Blottner/Eucken (Section 2.5.1) and the Gupta–Yos/CCS models (Section 2.5.2) to state-to-state species such that:

$$D_{sr_{vw}} = D_{sr} \tag{2.26a}$$

$$\mu_{s_v} = \mu_s \tag{2.26b}$$

$$\lambda_{k,s_v} = \lambda_{k,s} \tag{2.26c}$$

where s and r denote chemical species and v and w denote the corresponding sub-species (i. e.

vibrational levels).

Furthermore, a more detailed model is developed (State-Dependent Collisional Cross-Section Model in Section 2.5.2), in which the enhanced cross-sections of vibrationally excited molecules are accounted for.

2.5.1 Wilke/Blottner/Eucken Model

Wilke's Model [22] for gas mixture viscosities was developed through the application of the kinetic theory to the first order Chapman-Enskog relation. It is a mixing rule which assumes that all interactions between any particles present the same (hard sphere) cross-section [41]. It provides the transport coefficients for the chemical species. However, in order to couple this model to a state-resolved kinetic scheme, it was considered that the transport coefficient contribution of each sub-species v/w is equal to the transport coefficient contribution of the corresponding chemical species s/r (see Eqs. 2.26a-2.26c).

The gas mixture viscosity μ and the thermal conductivity λ_k for each global thermal energy mode are obtained using the following mixing rules:

$$\mu = \sum_v \frac{x_v \mu_s}{\phi_s} \qquad \lambda_k = \sum_v \frac{x_v \lambda_{k,s}}{\phi_s} \tag{2.27}$$

where x_v is the molar fraction of each sub-species v and μ_s represents the species individual viscosities. ϕ_s is a scale factor defined as:

$$\phi_s = \sum_r \left[1 + \sqrt{\frac{\mu_s}{\mu_r}} \left(\frac{M_r}{M_s}\right)^{\frac{1}{4}}\right]^2 \Bigg/ \sqrt{8\left(1 + \frac{M_r}{M_s}\right)} \tag{2.28}$$

where M_* represents each species' (s or r) molar mass. The species viscosities μ_s are obtained through curve fits determined by Blottner et al. [70]:

$$\mu_s(T_{tra,s}) = 0.1 \times \exp\Big((A_s \ln T_{tra,s} + B_s) \ln T_{tra,s} + C_s\Big) \tag{2.29}$$

where A_s, B_s and C_s are curve fitted coefficients for each species.

The thermal conductivity associated to each one of the thermal energy modes - $\lambda_{tra,s}$, $\lambda_{vib,s}$, $\lambda_{rot,s}$ and $\lambda_{el,s}$ - can be obtained using Eucken's relation [71].

$$\lambda_{tra,s} = \frac{5}{2} \mu_s C_{V_{tra,s}} \qquad \lambda_{k \neq tra,s} = \mu_s C_{V_{k,s}} \tag{2.30}$$

where $C_{V_{tra,s}}$ is the specific heat at a constant volume of species s in the translational energy mode.

The species mass diffusion coefficient is given by a single binary coefficient D assuming a constant Lewis number, Le = 1.2:

$$D_s = D = \frac{Le \lambda}{\rho C_P} \tag{2.31}$$

where C_P represents the gas mixture total specific heat at a constant pressure and λ represents the total thermal conductivity of the gas mixture. The Lewis number Le defines the ratio of the energy transport due to mass diffusion relative to that due to thermal conduction.

2.5.2 Gupta–Yos/Collision Cross-Section - Model 0

The Gupta–Yos model [23] is an approximate mixing rule that provides the transport coefficients for the chemical species. This model is a simplified form of the classical Chapman-Enskog solution for the Boltzmann equation system. It is assumed to be more accurate than the Wilke's Model, since it accounts for the true nature of the viscosity collision integrals by considering the corresponding collision cross-sections. However, it requires reasonably accurate collision integral data for each species pair in the gas mixture, thus it is not possible to implement this model if there is not sufficient data available.

In order to couple this model to a state-resolved kinetic scheme, it was considered that the transport coefficients of each sub-species v/w were equal to the transport coefficients of the corresponding chemical species s/r (see Eqs. 2.26a-2.26c). This model will be named *Model 0* for the purposes of this work.

The collision integrals ${\Delta_{sr}}^{(1)}$ and ${\Delta_{sr}}^{(2)}$ between species s and r are defined as function of the controlling temperature T_c:

$$\Delta_{sr}^{(1)} = \frac{8}{3}\left[\frac{2M_sM_r}{\pi R_u T_c(M_s+M_r)}\right]^{1/2} \pi{\overline{\Omega}_{sr}}^{(1,1)}(T_c)\times 10^{20} \tag{2.32}$$

$$\Delta_{sr}^{(2)} = \frac{16}{5}\left[\frac{2M_sM_r}{\pi R_u T_c(M_s+M_r)}\right]^{1/2} \pi{\overline{\Omega}_{sr}}^{(2,2)}(T_c)\times 10^{20} \tag{2.33}$$

where $\pi{\overline{\Omega}_{sr}}^{(1,1)}$ and $\pi{\overline{\Omega}_{sr}}^{(2,2)}$represent weighted averages of the cross-sections, which are evaluated as curve fits to the tabular data generated in [72]. The controlling temperature T_c in Eqs. 2.32 and 2.33 depends on the type of particles colliding. It refers to the heavy-species translational temperature $T_{tra,h}$, except if the collision involves an electron, in which case the electron temperature $T_{el} = T_{tra,el}$ should be used.

For the calculation of the gas mixture viscosity, the following equation is used:

$$\mu = \sum_v \frac{m_s x_v}{\sum\limits_w x_w \Delta_{sr}^{(2)}} \tag{2.34}$$

where m_s is the sth species mass. The translational mode of heavy species λ_{tra} and electrons λ_e are defined as:

$$\lambda_{tra} = \frac{15}{4}k_B \sum_{v\neq e} \frac{x_v}{\sum\limits_w \alpha_{s,r} x_w \Delta_{sr}^{(2)}(T_{tra})} \qquad \lambda_e = \frac{15}{4}k_B \frac{x_e}{\sum\limits_w \alpha_{e,r} x_w \Delta_{er}^{(2)}(T_{vib})} \tag{2.35}$$

where k_B is the Boltzmann constant and $\alpha_{s,r}$ is given by:

$$\alpha_{s,r} = 1 + \frac{[1 - M_s/M_r][0.45 - 2.54(M_s/M_r)]}{[1 + (M_s/M_r)]^2} \tag{2.36}$$

The global thermal conductivities associated with the rest of the heavy species energy modes, λ_{rot}, λ_{vib}, λ_{exc} are defined as:

$$\lambda_{rot} = \sum_{v=m} \frac{x_v m_s C_{V_{rot,s}}}{\sum\limits_{w} x_w \Delta_{sr}^{(1)}} \qquad \lambda_{vib} = \sum_{v=m} \frac{x_v m_s C_{V_{vib,s}}}{\sum\limits_{w} x_w \Delta_{sr}^{(1)}} \qquad \lambda_{exc} = \sum_{v} \frac{x_v m_s C_{V_{exc,s}}}{\sum\limits_{w} x_w \Delta_{sr}^{(1)}} \tag{2.37}$$

where m denotes a molecular species. In thermal equilibrium, the total thermal conductivity λ is given by:

$$\lambda = \lambda_{tra} + \lambda_e + \lambda_{rot} + \lambda_{vib} + \lambda_{exc} \tag{2.38}$$

In thermal nonequilibrium, the thermal conductivity associated with each thermal energy mode is calculated by considering the individual contributions of each species to that same mode, according to the multi-temperature model under consideration.

The mass diffusion coefficient D_{sr} defines the diffusion velocity of each species relative to the different species and reads:

$$D_{sr} = \frac{k_B T_c}{p \Delta_{sr}^{(1)}} \tag{2.39}$$

The effective diffusion coefficient D_s is determined by considering the multi-component mixture as a binary mixture consisting of species s and a composite species that represents the contribution of the remaining species. It is given by:

$$D_s = \frac{1 - x_s}{\sum\limits_{r \neq s} \frac{x_r}{D_{sr}}} \tag{2.40}$$

For a single species mixture, its properties are determined as follows:

$$\mu_s = \frac{5}{16} \frac{\sqrt{\pi m_s k_B T_c}}{\pi \overline{\Omega}_{sr}^{(2,2)}} 10^{20} \tag{2.41}$$

$$\lambda_{tra,s} = \frac{75}{64} k_B \frac{\sqrt{\pi k_B T_c / m_s}}{\pi \overline{\Omega}_{sr}^{(2,2)}} 10^{20} \tag{2.42}$$

$$\lambda_{rot,s=m} = \frac{8}{3} k_B C_{V_{rot,s}} \frac{\sqrt{\pi k_B T_c m_s}}{\pi \overline{\Omega}_{sr}^{(1,1)}} 10^{20} \tag{2.43}$$

$$\lambda_{vib,s=m} = \frac{8}{3} k_B C_{V_{vib,s}} \frac{\sqrt{\pi k_B T_c m_s}}{\pi \overline{\Omega}_{sr}^{(1,1)}} 10^{20} \tag{2.44}$$

$$\lambda_{exc,s\neq e} = \frac{8}{3} k_B C_{V_{exc,s}} \frac{\sqrt{\pi k_B T_c m_s}}{\pi \overline{\Omega}_{sr}^{(1,1)}} 10^{20} \tag{2.45}$$

where μ_s represents the viscosity for one species s, $\lambda_{tra,s}$ the translational thermal conductivity and

$\lambda_{rot,s}$, $\lambda_{vib,s}$ and $\lambda_{exc,s}$ represent the internal energy modes thermal conductivity. Consequently, the total thermal conductivity for a single species mixture is:

$$\lambda_s = \lambda_{tra,s} + \lambda_{rot,s} + \lambda_{vib,s} + \lambda_{exc,s} \tag{2.46}$$

State-Dependent Collisional Cross-Section Correction - Model 1

As discussed above, transport models rely among another things on adequate microscopic collisional cross-sections. To account for the fact that vibrationally excited molecules have larger internuclear distances (and hence larger cross-sections), a semi-empirical correction is implemented in this work, which will be dubbed *model 1*. In this model, the collision cross-sections for the chemical species calculated with the Gupta–Yos/CCS model are corrected by a state-specific factor that depends on the vibrational level of a molecule.

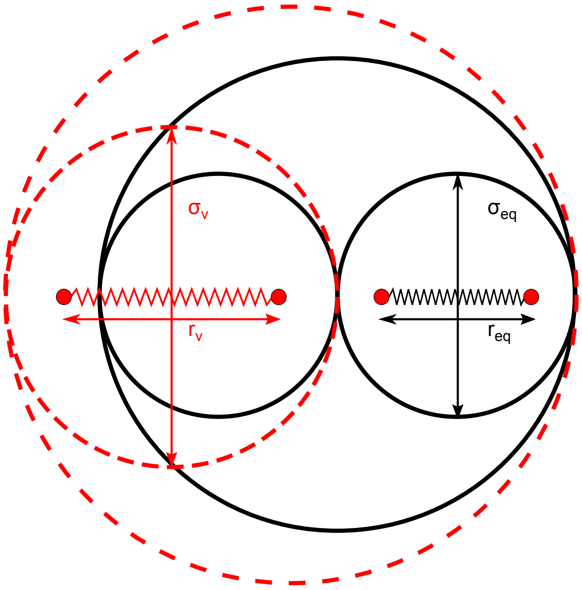

Figure 2.5: Cross-section diameter increase of vibrationally excited molecules.

This model ccounts for the enhancement of the average collision cross-sections $\overline{\Omega}_{sr}^{(1,1)}$ and $\overline{\Omega}_{sr}^{(2,2)}$ in the Gupta–Yos model according to:

$$\overline{\Omega}_{sr}^{(1,1)} = \overline{\Omega}_{sr}^{(1,1)} \times \frac{\Omega_{CD(w)}^{AB(v)}}{\Omega_{CD(0)}^{AB(0)}} \tag{2.47}$$

$$\overline{\Omega}_{sr}^{(2,2)} = \overline{\Omega}_{sr}^{(2,2)} \times \frac{\Omega_{CD(w)}^{AB(v)}}{\Omega_{CD(0)}^{AB(0)}} \tag{2.48}$$

where $\Omega_{CD(w)}^{AB(v)}$ is the hard-sphere collisional cross-section between the (v) vibrational level of diatom AB and the (w) vibrational level of diatom CD, $\Omega_{CD(0)}^{AB(0)}$ is the hard-sphere collisional cross-section between the ground level of diatom AB and the ground level of diatom CD.

For diatom-diatom collisions, we have:

$$\Omega^{AB(v)}_{CD(w)} = \pi\Big(\frac{\sigma^{AB}_{v} + \sigma^{CD}_{w}}{2}\Big)^2 \tag{2.49}$$

For atom-diatom collisions, we have:

$$\Omega^{AB(v)}_{CD(w)} = \pi\Big(\frac{\sigma^{AB}_{v} + \sigma^{C}}{2}\Big)^2 \tag{2.50}$$

In Eq. 2.50, σ is the interaction distance, which equals the sum of the internuclear distance and the electron cloud distance:

$$\sigma^{AB(v)} = r^{AB}_{v} + (\sigma^{AB}_{eq} - r^{AB}_{v=0}) \tag{2.51}$$

where $r^{AB}_{v=0}$ is the internuclear distance of the ground level, σ^{AB}_{eq} is the low-velocity interaction distance [73] and r^{AB}_{v} is the internuclear distance for higher v-levels.

Chapter 3

Numerical Methodology and Setup

The largest part of the work load for this project comprises the implementation of the transport models presented in the previous chapter in an existing computer program. SPARK code is the numerical solver used in the present thesis. It is an in-house code previously developed by Lopez et al. [12] tailored for hypersonic flow simulations. The SPARK code is capable of simulating compressible Euler and Navier-Stokes reactive flow simulations by means of detailed kinetic models. As previously discussed in Chapter 2, full Navier-Stokes reactive flow numerical simulations require modelling gas mixture average diffusive effects and transport coefficients for each species in the mixture. The problem becomes more challenging when state-specific models are considered for the gas description. In this case, each vibrational, rotational and/or electronic state is treated as a pseudo-species in the system of governing equations and therefore, a continuity equation and the respective transport coefficients must be defined for these states. So far, SPARK only allowed solving state-specific gas description models if Euler governing equations where considered. A particular contribution of this thesis was the extension and testing of the capabilities of SPARK solver to allow full Navier-Stokes simulations considering a state-specific gas internal energy description, by devising transport models for the species internal states.

Section 3.1 contains a general overview of SPARK's structure, the programming strategy adopted in this work and a summary of the numerical methods used by the solver. In Section 3.2, databases are defined to allow a consistent comparison between results provided by multi-temperature and state-to-state simulations. Finally, Section 3.3 presents the setup of the simulations performed.

3.1 SPARK Solver

SPARK - Software Package for Aerodynamics, Radiation and Kinetics - is the name of the CFD code used throughout this work. It is maintained in IPFN (Instituto de Plasmas e Fusão Nuclear) at Instituto Superior Técnico. The code was developed with the objective of simulating nonequilibrium hypersonic flows with high adaptability to the user needs. Steady or unsteady inviscid and viscous flow simulations are available, as the code includes both the Euler and the Navier-Stokes formulations. Furthermore, SPARK provides stand-alone solvers dedicated to standing shock, perfect gas, frozen gas or reactive gas flow simulations, as well as mesh refinement tools for shock and/or boundary layer capturing.

3.1.1 Structure

Given the multiphysics nature of hypersonic flows, SPARK takes advantage of the object-oriented programming techniques of the Fortran 03/08 language - data abstraction, encapsulation, inheritance, polymorphism and operator overloading - to focus its design and implementation on modularity and maintainability, providing a clear separation between physical models and numerical methods. The object-oriented programming philosophy allows to strictly separate different components of the solver into independent modules which share a common data structure, facilitating both inter-module communication and easy integration of new functionalities. Furthermore, each physical quantity and physical model is represented by an object. This leads to a direct translation of the physical representation of each quantity into the programming language, without any intermediate representation. A diagram that represents the main structure of the code is shown in Fig. 3.1.

Figure 3.1: Main structure of the SPARK code [12]

As illustrated in Fig. 3.1, in order to run a simulation in code SPARK, an input file is required. A detailed list of SPARK inputs is presented in Appendix C, in Section C.1. Furthermore, a detailed description of the relevant objects and procedures - regarding transport models and state-to-state models - is given below.

Transport Models

The `Gas` object contains all the physics of the flow, which means that it encapsulates the objects associated with the different physical models. Accordingly, the procedures used to compute transport properties are contained in the `Transport` object, which is encapsulated in the `Gas` object. In the `Transport` object, the procedures used to compute transport coefficients are available to the user of the program. The user of the `Transport` object, in the context of a full hypersonic flow simulation, is SPARK's `Gas` object, since it is responsible for the computation of all the gas properties. Alternatively, the user can also be any other application code built to generate specific results for verification analysis.

The public procedures contained in the `Transport` object are:

- `Construct` - Allocates in memory and defines the necessary variables according to the user input, setting up the `Transport` object for later use.

- `Set_Model` - Sets the transport model to be used according to the user input: Wilke/Blottner/Eucken (macroscopic) or Gupta–Yos/CCS (macroscopic) - transport models available before any implementation is carried out.
- `Compute_Transport` - Computes all the transport properties for all the species simultaneously, μ, λ_k and D_s.
- `Compute_Viscosity` - Computes the mixture viscosity coefficient μ.
- `Compute_ThermalCond` - Computes the thermal conductivity coefficient for each thermal energy mode λ_k.
- `Compute_MassDiffusion` - Computes the diffusion coefficient of each species D_s.

The procedures used to compute individual transport properties are available for the mere purpose of convenience, since only the general procedure `Compute_Transport` is optimized for performance, provided that it is used in full-scale simulations.

Independently of the transport model being used, the `Compute_Transport` procedure has the following inputs and outputs:

- Inputs: `mixture`, ρ, c_s, T_k, P_k, Cp_k
- Outputs: μ, λ_k and D_{sr}

where ρ is the density, c_s and D_s are, respectively, the mass fraction and the mass diffusion coefficient of species s, T_k, P_k, Cp_k and λ_k are, respectively, the temperature, pressure, specific heat at constant pressure and thermal conductivity of the energy mode k, μ is the mixture viscosity and `mixture` is the object where all the empirical and pre-processed thermodynamic data related to the species is contained. The subscripts k and s denote the dimensions of vectors and matrices and depend on the multi-temperature model being used and the number of species in the mixture.

The arrangement of the `Transport` object allows it to be independent of the specific model being used, i. e., it only defines an interface for a generic transport model. The actual implementation of a specific transport model is done in independent submodules. Each submodule is then associated with a different `Transport_Strategy` object, in which the implementation of the each transport model is done using normal procedural programing techniques.

State-to-State Models

The objects associated with the chemical species and the internal energy levels of the chemical species are encapsulated in the `Mixture` object, also contained in the `Gas` object. The structure of these objects is defined in such a way that allows the modelling of the chemical species either using the equilibrium Boltzmann statistics (used in the multi-temperature approach) or, alternatively, the state-specific approach. Specifically, a list of objects corresponding to a generic set of chemical species is defined.

Each `Chemical Species` object encapsulates a nested structure of internal levels, which comprises the electronic, vibrational and rotational sets of levels. A representation of this structure is shown in Fig. 3.2.

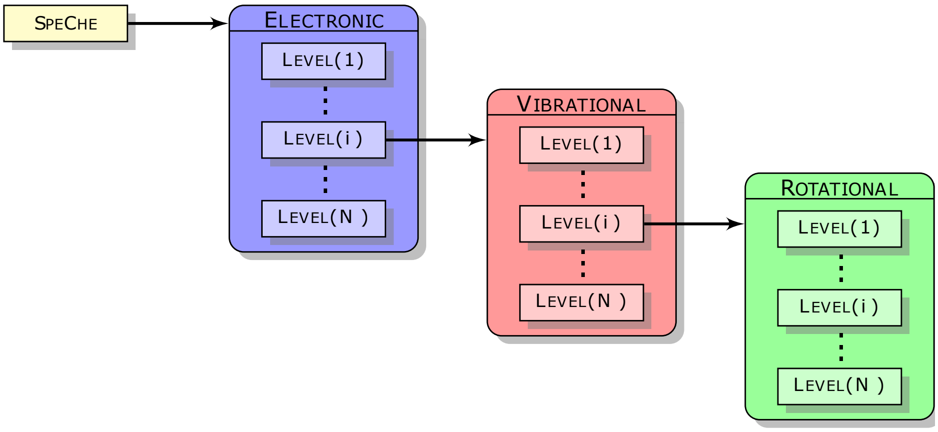

Figure 3.2: Illustration of the internal structure of chemical species [12]

Furthermore, a list of objects that represents a generic set of total species is similarly defined. In the case of Boltzmann distributions over the internal energy levels, this list is the same as the list of chemical species. Alternatively, in the modelling of nonequilibrium with the state-to-state approach, the list of total species matches the set of the corresponding internal levels, which are treated as pseudo-species. A mapping between the two lists is illustrated in Fig. 3.3 for the different possible cases.

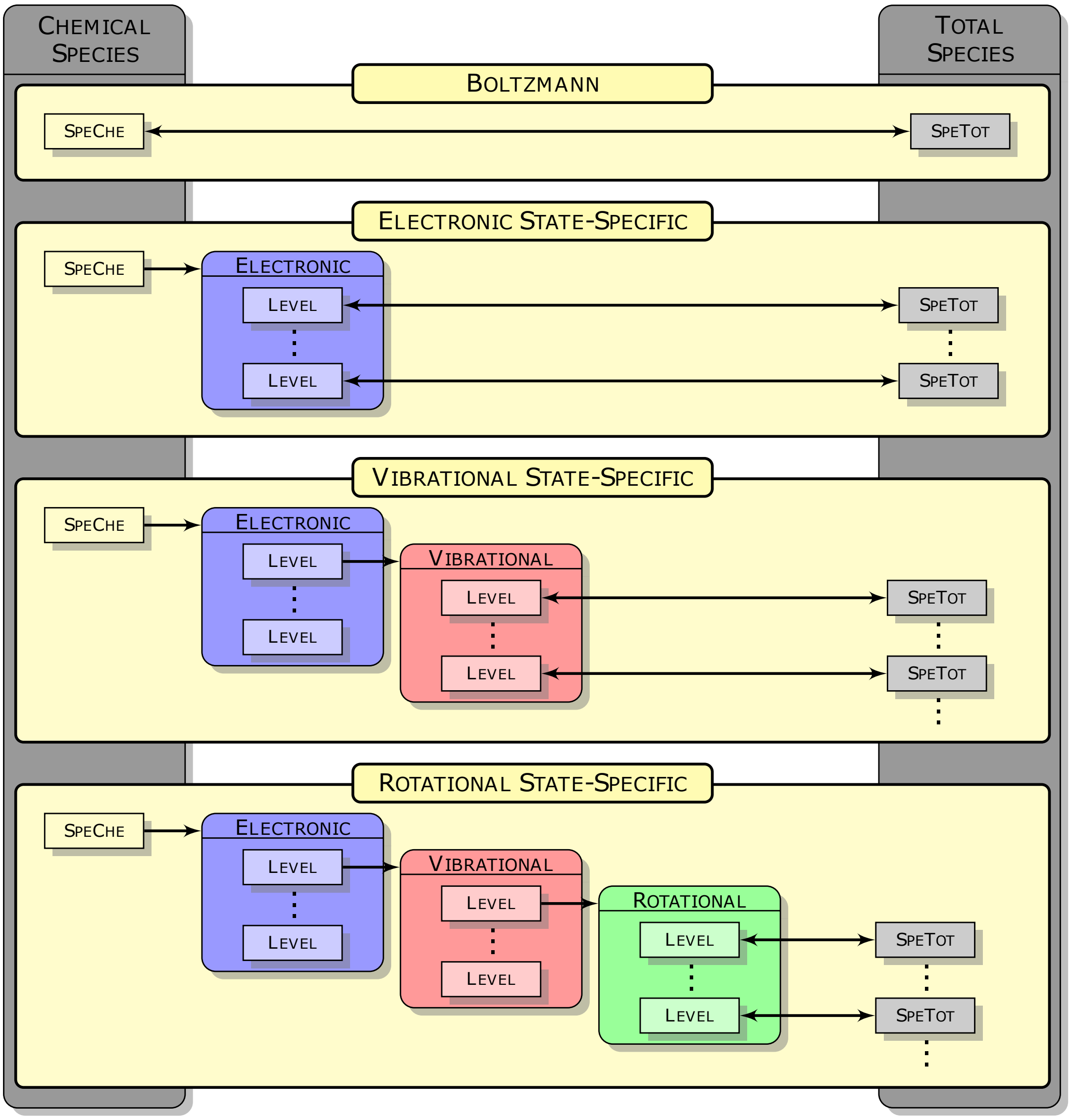

Figure 3.3: Illustration of the mapping scheme for the internal modes of a chemical species [12]

Up to this point, the code allowed running Navier-Stokes only in the case of equilibrium Boltzmann distributions over the internal levels of the chemical species. All the variables and procedures associated to the calculation of transport coefficients and dissipative fluxes were operating with the list of chemical species. Section 3.1.2 describes the strategy used for the implementation of state-specific transport coefficients, to allow the coupling of dissipation phenomena to the state-to-state approach.

3.1.2 Programming Strategy

The implementation of transport coefficients for non-Boltzmann distributions was conducted in two stages. Firstly, macroscopic transport models suited for the multi-temperature approach were adapted to state-to-state species according to Sections 2.5.1 and 2.5.2. Secondly, the state-specific transport model described in Section 2.5.2 was implemented.

Wilke/Blottner/Eucken and Gupta–Yos/CCS Models Adapted to State-to-State

To begin with, the code was adapted to account for the internal levels of chemical species (sub-species) in all of the objects and modules related to the calculation of dissipative fluxes and corresponding transport coefficients. This means that the associated procedures were adapted to operate with the list of total species. Furthermore, the contribution of each sub-species to the mixture's transport coefficients was set to the value of the equilibrium transport contribution of the corresponding chemical species, weighted by the molar fraction of the sub-species (as described in Sections 2.5.1 and 2.5.2). Hence, the transport coefficients of the sub-species are calculated as function of the collision cross-sections of the corresponding chemical species. Given the mapping between the chemical and total species lists (Fig. 3.3), after the implementation described above, procedures associated with the calculation of dissipative fluxes are able to operate with both Boltzmann and non-Boltzmann level distributions. If the case of Boltzmann distributions is considered, transport coefficients are determined according to the macroscopic Wilke/Blottner/Eucken or the Gupta–Yos/CCS model, suited for a multi-temperature description. On the other hand, if the case of non-Boltzmann distributions is considered, state-specific transport coefficients are determined according to Sections 2.5.1 (Wilke/Blottner/Eucken Model adapted to state-to-state) and 2.5.2 (Gupta–Yos/Collision Cross-Section Model adapted to state-to-state).

State-Dependent Collisional Cross-Section Model Update

At a later stage, the State-Dependent Collisional Cross-Section correction (detailed in Section 2.5.2) was implemented on the Gupta–Yos transport model. A new submodule was created to be associated with the corresponding `Transport_Strategy` object, in which the necessary procedures were defined. Specifically, in the procedure `Compute_Transport`, the procedure for computing collision cross-sections provided by the Gupta–Yos/CCS transport strategy adapted to state-to-state is called. The values of the collision cross-sections are then corrected according to Section 2.5.2. The state-specific correction factors are determined in the `Total Species` object, under the condition of non-Boltzmann distributions (number of total species $>$ number of chemical species). Once the enhanced cross-sections of excited molecules are determined, the calculation of state-specific transport coefficients follows the Gupta–Yos/CCS strategy adapted to state-to-state.

After this programming strategy was implemented in SPARK, the code was capable to run full state-to-state Navier-Stokes simulations.

3.1.3 Numerical Methods

The `Flow` object contains all the numerical methods used for the numerical implementation of the physical models detailed in the previous chapter. The numerical resolution of the system of Eqs. 2.1a-2.1d is obtained by means of the Finite Volume Method (FVM). This method consists in discretizing the computational domain into small control volumes (cells), ensuring the conservation of conservative quantities in each individual volume. Variables are defined in the centre of each cell and the communication between cells is made by their respective faces. With regard to temporal discretization, both second-order explicit and implicit time integration schemes are available in SPARK. Diffusive fluxes are discretized using standard second-order central finite-differences. More attention must be paid to the discretization of convective fluxes in hyperbolic flows simulations, due to the existence of strong discontinuities in primitive variables. Therefore, the computation of each cell's convective fluxes is achieved by the solution of a Riemann's problem, at the cells interfaces. The SPARK code discretizes convective terms on the basis of Roe's approximate Riemann solver, using the second-order Harten-Yee scheme [60]. Variables are evaluated at the cell's faces with Roe averages between the left and right states. Furthermore, in order to avoid numerical oscillations the minmod flux limiter is applied to characteristic variables.

3.2 State-to-State and Multi-Temperature Database Definition

Performing a valid comparison between state-to-state and multi-temperature simulations for a N_2/N flow implies comparing simulations that resort to the same consistent chemical, thermodynamic and transport databases, with only the physical models differing. Therefore, when imposing a Boltzmann distribution over the vibrational levels of N_2, the state-specific databases should be reduced to the macroscopic ones used in multi-temperature simulations.

3.2.1 Kinetics

With regard to kinetics, the Air5-STELLAR scheme is used throughout this work. It provides the most up to date state-resolved dissociation datasets for N_2–N_2 [74] and N_2–N [75] collisions, on the basis of the FHO model (Section 2.3.1). Lino da Silva et al. reduced these sets to two-temperature and one-temperature rates by summing the state-specific dissociation rates $k(v,T)$ weighted by the relative populations of each vibrational level, after imposing a Boltzmann distribution at a given temperature T or T_{vib}. For two-temperature rates:

$$k(T,T_{vib}) = \sum_v k(v,T)\frac{N_v}{\sum_v N_v} \tag{3.1}$$

In equilibrium, for one-temperature rates:

$$k^0(T) = (T, T_{vib} = T) \tag{3.2}$$

This method yields what we call the Air5-STELLAR-Boltzmann kinetic scheme, employed in multi-temperature simulations carried out in this work.

3.2.2 Energy Exchange

In terms of databases for energy exchange, the Losev model for Boltzmann distributions (Section 2.4) was utilized in this work for the two-temperature simulation. However, in order to perform a coherent comparison with results obtained from state-to-state simulations, coefficients $A^L_{s,r}$, $B^L_{s,r}$, $C^L_{s,r}$ and $D^L_{s,r}$ were fitted for N_2-N_2 and N_2-N collisions from the FHO model summarized in section 2.3.1. The obtained polynomial fit is illustrated in Fig. 3.4:

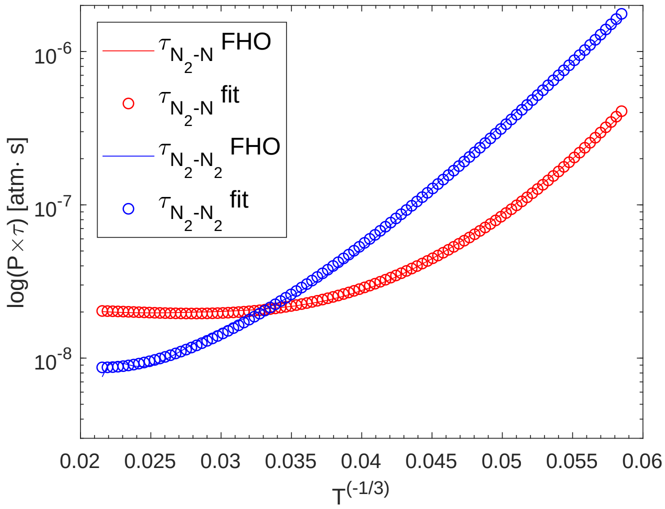

Figure 3.4: Vibrational relaxation times for N_2-N_2 and N_2-N collisions: Losev model and polynomial fit from the FHO model.

The polynomial fit expression yielded the following values:

- N_2-N_2 collisions: $A = -26.5867$, $B = 166.2004$, $C = 609.4595$, $D = 0.089696$.
- N_2-N collisions: $A = -9.5503$, $B = -342.2877$, $C = 4661.7908$, $D = -0.063586$.

3.2.3 Transport

As for transport properties, a database was defined for the cross-section size of vibrationally excited molecules, to be used in the State-Dependent Collisional Cross-Section model (Section 2.5.2). Regarding the N_2/N mixture studied in this work, values for the internuclear distances r^{AB}_v and $r^{AB}_{v=0}$ for N_2 were determined using the RKR method [76]. The obtained results are illustrated by the potencial energy curve in Fig. 3.5.

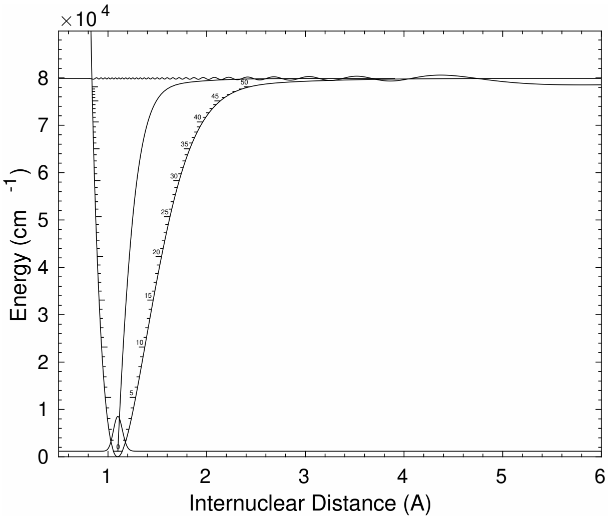

Figure 3.5: Potencial curve for the N_2 molecule

The resulting data is presented in Table B.1 of Appendix B. Furthermore, values for the equilibrium interaction distances σ_{eq}^{AB} for N_2 and σ_{eq}^{C} for N were taken from [73]: $\sigma_{eq}^{AB} = 3.798$ Å and $\sigma_{eq}^{C} = 3.298$ Å. It should be noted that, for N(1), $\sigma^{C} = \sigma_{eq}^{C}$, since it is not a molecular species.

3.3 Test-Cases Setup

A set of numerical experiments has been set up in order to better understand the impact of the formulated transport models. These experiments are divided into two groups. The first set of simulations is designed to perform verification of these models and compare them against the models already implemented in SPARK, by means of conducting 0D equilibrium computations. Ultimately, results provided from this first set of simulations will help understand and discuss results obtained in multidimensional simulations. The second set of numerical experiments is designed to mimic a practical case of a sphere entering the Earth's atmosphere. This second set of simulations will allow to compare the impact of using different transport models in multidimensional reentry simulations.

3.3.1 Equilibrium 0D Computations - Transport Model Assessment

In order to ascertain if the implemented transport models are in accordance with the conceptual models and in order to assess the extent to which the resulting code can be properly used for analysis, code verification and comparison tests were conducted.

An application code was developed to compute transport coefficients as function of the temperature, using only the `Gas` object. The equilibrium concentrations of the species were computed for a N_2/N mixture at atmospheric pressure and a range of temperatures between 500 K and 50$\times 10^3$ K. Transport coefficients were obtained for these input data, in order to pinpoint their dependence on the modelling of internal energy modes and thermodynamic characteristics.

A set of test-cases has been performed. The setup of the different test-cases is shown in Table 3.1:

Table 3.1: Test-cases considered in equilibrium 0D computations

	Internal Modes Description Model	**Transport Model**
Test-case 1	Boltzmann	Wilke/Blottner/Eucken
Test-case 2	Boltzmann	Gupta–Yos/CCS
Test-case 3	Vibrational state-specific	Model 0
Test-case 4	Vibrational state-specific	Model 1

Test-case 1

In Test-case 1, the populations of the internal levels of energy are described by a Boltzmann distribution. This means that transport coefficients are defined for each chemical species, using the macroscopic Wilke/Blottner/Eucken transport model.

Test-case 2

In Test-case 2, similarly to Test-case 1, the populations of the internal levels of energy are described by a Boltzmann distribution. However, for this case, the transport coefficients for each chemical species are obtained using the macroscopic Gupta–Yos/CCS model.

Test-case 3

In Test-case 3, the N_2 internal energy modes are described by a vibrational state-specific model. This implies that, for the mixture considered in this work, transport coefficients are calculated for each vibrational level of N_2. To that end, the Gupta–Yos/CCS model adapted to state-to-state species (referred to as *Model 0* - Section 2.5.2) is used.

Test-case 4

Similarly to Test-case 3, in Test-case 4, the N_2 internal energy modes are also described by a state-specific vibrational model. However, in this case, transport coefficients for the vibrational levels of N_2 are calculated with the State-Dependent Collisional Cross-Section model (referred to as *Model 1* - 2.5.2), which takes into account the increased diameter of vibrationally excited molecules.

The results generated by these tests are presented and discussed in Section 4.1. The objectives are: (a) to understand the impact of using non-Boltzmann distributions in the computation of transport coefficients (Test-cases 1 and 2 vs. Test-case 3); (b) to evaluate the influence of accounting for the increased cross-sections of vibrationally excited molecules (Test-case 3 vs. Test-case 4).

3.3.2 Multidimensional Computations - Impact of State-to-State Transport Models in 2D simulations

To assess the impact of state-specific transport models in the two-dimensional study of reentry flows, seven different simulations were performed for a simple case study. The previously described formulation has been applied to a two-dimensional nitrogen flow past a sphere with radius $r = 0.1524$ m, at v=7km/s, pressure 27 Pa and variable temperature. The mixture considered in this work consists of 61 vibrational levels for the N_2 molecule and 1 electronic level for atomic nitrogen N.

Computational Challenges in 2D simulations

As previously discussed in Chapter 1, the coupling of state-to-state kinetics to fluid dynamic equations poses a considerable challenge in terms of computational costs. In the context of a full hypersonic flow simulation, a large number of mass conservation equations (one per internal energy level of each chemical species - sub-species) must be numerically solved. Furthermore, the determination of transport properties (also for every sub-species) requires the computation of collision cross-sections for every pair of sub-species, in each iteration.

To overcome this problem and accelerate convergence, all two-dimensional state-to-state viscous simulations used the Wilke/Blottner/Eucken model adapted to state-to-state species (Section 2.5.1) at the initial stage. The simplicity of the Eucken's relation and the assumption of a constant Lewis number are obviously computationally less expensive than the more detailed mixing rules of the Gupta–Yos/CCS model adapted to state-to-state species (Section 2.5.2), which account for collision cross-sections. In fact, previous work conducted by Loureiro [77] showed that, for Boltzmann distributions, the computation of transport coefficients with the Gupta–Yos/CCS model uses up to twice the CPU time of the Wilke/Blottner/Eucken model.

Test-Cases

The setup of the seven simulations is shown in Table 3.2:

Table 3.2: Test-cases considered in 2D simulations

	Internal Modes Description Model	**Transport Model**	**Kinetic Scheme**	**T_∞ [K]**
Test-case 1	Boltzmann (One-temperature)	Gupta–Yos/CCS	Air5-STELLAR-Boltzmann	300
Test-case 2	Boltzmann (Two-temperature)	Gupta–Yos/CCS	Air5-STELLAR-Boltzmann	300
Test-case 3	Vibrational state-specific	- (Euler)	Air5-STELLAR	300
Test-case 4	Vibrational state-specific	Model 0	Air5-STELLAR	300
Test-case 5	Vibrational state-specific	Model 1	Air5-STELLAR	300
Test-case 6	Vibrational state-specific	Model 0	Air5-STELLAR	700
Test-case 7	Vibrational state-specific	Model 1	Air5-STELLAR	700

Test-case 1

In Test-case 1, a one-temperature simulation with T_∞ = 300 K is carried out. This is the most simple approximation of a multi-temperature model, in which thermal equilibrium is assumed, that is, one temperature only:

$$T_{tra,s} = T_{vib,s} = T_{rot,s} = T_{el,s} = T \tag{3.3}$$

Since the four thermal modes are considered to be in equilibrium, there is no energy exchange between them and Eq. 2.1d vanishes.

The populations of the internal levels are described by Boltzmann distributions. Transport coefficients of chemical species are calculated considering the macroscopic Gupta–Yos/CCS model. Moreover, the Air5-STELLAR-Boltzmann kinetic scheme is used, in which chemical reactions and dissociation rates are detailed for chemical species.

Test-case 2

For Test-case 2, a two-temperature simulation with T_∞ = 300 K is performed. The two-temperature model, proposed by Park [78], refers to a more detailed approximation, which accounts for the coupling of chemical and vibrational nonequilibrium. This is achieved by means of considering translational and vibrational energy modes for the molecules and the corresponding energy transfer processes between the two, as well as vibration-dissociation processes for the formation of atoms. In this regard, two temperatures (T_{tra}, T_{vib}) are defined: T_{tra} characterizes the translational energy of the atoms and molecules and T_{vib} characterizes that vibrational energy of the molecules. This model further assumes that the molecular rotational mode is in equilibrium with the translational one and that the translational mode of the electrons and the electronic excitation mode of atoms and molecules are in equilibrium with the molecular vibrational mode:

$$T_{rot} = T_{tra} \quad \text{and} \quad T_{vib} = T_e = T_{exc} \tag{3.4}$$

Similarly to Test-case 1, in Test-case 2 the populations of the internal levels are also described by Boltzmann distributions. Transport coefficients of chemical species are calculated considering the macroscopic Gupta–Yos/CCS model. Moreover, the Air5-STELLAR-Boltzmann kinetic scheme is used, in which chemical reactions and dissociation rates are detailed for chemical species.

Test-case 3

Test-case 3 refers to an inviscid Euler state-to-state simulation with T_∞ = 300 K. It considers non-Boltzmann distributions for which each vibrational state of the N_2 molecule as well as the first electronic level of atomic nitrogen N(1) are treated as pseudo-species. The Air5-STELLAR kinetic scheme is used, in which reactions and dissociation rates are detailed for the vibrational levels $N_2(v)$.

Test-case 4

Test-case 4 refers to a Navier-Stokes state-to-state simulation with T_∞ = 300 K. Distributions for the populations of $N_2(v)$ vibrational levels as well as the kinetic scheme are defined as in Test-case 3. The transport coefficients of sub-species are obtained with the transport model Gupta–Yos/CCS adapted to state-to-state species (referred to as *Model 0* - Section 2.5.2).

Test-case 5

Test-case 5 also refers to a Navier-Stokes state-to-state simulation with T_∞ = 300 K. Distributions for the populations of $N_2(v)$ vibrational levels as well as the kinetic scheme are defined as in Test-cases 3 and 4. Regarding transport properties, the enhanced cross-sections of vibrationally excited N_2 are taken into account by means of employing the State-Dependent Collisional Cross-Section model (referred to as *Model 1* - Section 2.5.2).

Test-cases 6 and 7

Finally, Test-cases 6 and 7 are equivalent to Test-cases 4 and 5, respectively. However, the upstream temperature changes to T_∞ = 700 K. This is relevant for the simulation of experiments where the freestream might be hotter than the ambient temperature (such as in the case of blow-off hypersonic nozzles).

The results provided by these simulations are presented and discussed in Section 4.2. The objectives are: (a) to compare results of a full state-to-state Navier-Stokes simulation with those provided from Navier-Stokes multi-temperature simulations (Test-case 4 vs Test-case 1 and 2) (b) to assess the impact of accounting for transport phenomena in state-to-state simulations (Test-case 3 vs. Test-case 4); (c) to evaluate the influence of taking into account the increased cross-sections of N_2 vibrational levels in state-to-state viscous flow simulations (Test-case 4 vs. Test-case 5); (d) to assess the impact of the freestream temperature in Navier-Stokes state-to-state simulations(Test-case 6 vs. Test-case 7).

Mesh and Boundary Conditions

Given the axisymmetry condition of the problem and since it is assumed that the convective heat fluxes are negligible in the low-density afterbody region (a reasonable assumption shared by the works presented in the state-of-the-art), only half of the front body was considered in the computational domain.

For all simulations, the same boundary conditions were applied. Furthermore, a structured mesh consisting of 60 elements in the direction normal to the capsule's surface and 60 elements in the direction parallel to the capsule's surface was used. Regions where higher gradients are present - shock-layer and boundary-layer - were coarsely refined. Figure 3.6 illustrates the type of mesh used together with the boundary conditions:

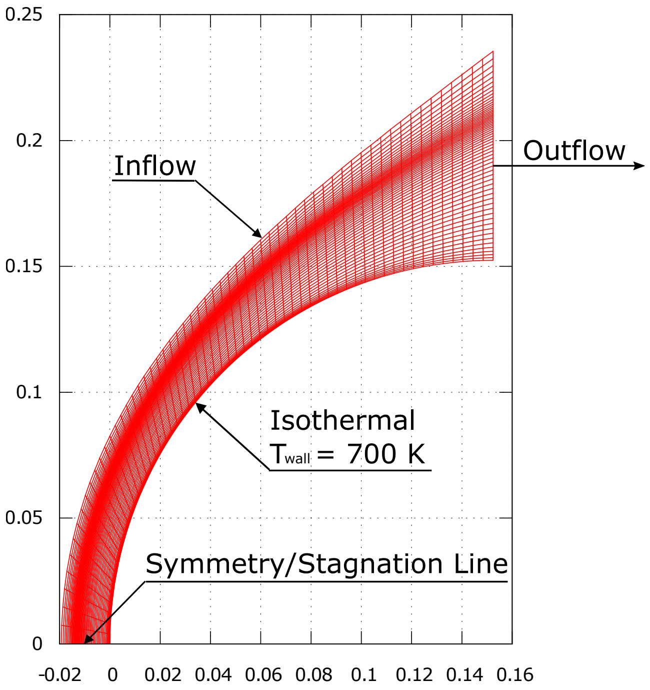

Figure 3.6: Illustration of the mesh and boundary conditions considered for the CFD domain.

The upstream conditions for Test-cases 1-5, given in Table 3.3, were taken from Josyula et al. [79], for a freestream velocity of 7km/s.

Table 3.3: Upstream conditions for Test-cases 1-5 from [79]

T_∞ [K]	P_∞ [Pa]	V_∞ [km/s]	Mass Fractions [-]
300	27	7	N_2:1

The upstream conditions for Test-cases 6-7, given in Table 3.4, for a freestream velocity of 7 km/s:

Table 3.4: Upstream conditions for Test-cases 6-7

T_∞ [K]	P_∞ [Pa]	V_∞ [km/s]	Mass Fractions [-]
700	27	7	N_2:1

Chapter 4

Results

This chapter presents the results obtained from numerical experiments using the physical models and corresponding implementation described, respectively, in Chapters 2 and 3. In Section 4.1, a qualitative comparison between the different transport models is conducted. The same transport models were then applied to a 2D case study, for which results are shown and discussed in Section 4.2.

4.1 Transport Model Assessment

As described in Section 3.3.1, gas transport properties are computed considering Wilke and Gupta models, Model 0 and Model 1 as a function of the gas temperature, in the range of 500 to 50,000 K. These results were obtained assuming the equilibrium composition of a N_2/N mixture at each value of the gas temperature (500 up to 50,000 K) and ambient pressure. The equilibrium composition of the mixture is shown in Fig. 4.1, for the sake of the results discussion that follows.

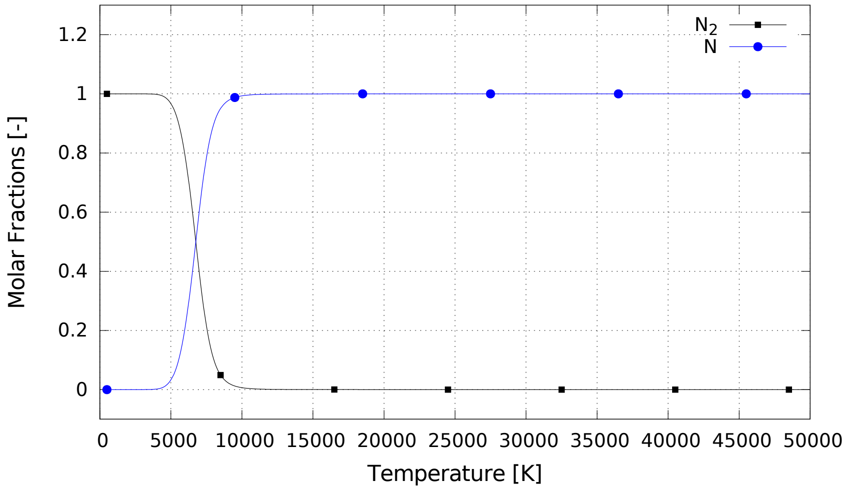

Figure 4.1: Equilibrium composition of N_2/N mixture, 1 atm.

Figure 4.1 shows that, in equilibrium conditions, there is no dissociation of N_2 for $T < 4{,}000$ K, whereas, for $T > 9{,}000$ K, N_2 becomes completely dissociated. From T = 4,000 K up to T = 9,000 K,

N_2 molar fraction decreases while N molar fraction naturally increases. At T = 6,000 K, both N_2 and N molar fractions are 0.5. This value of the gas temperature will be important in the analysis of transport coefficients that follows. For this analysis, Fig. 4.2 shows the evolution of the mixture a) viscosity, b) thermal conductivity and c) the N_2 mass diffusion coefficient.

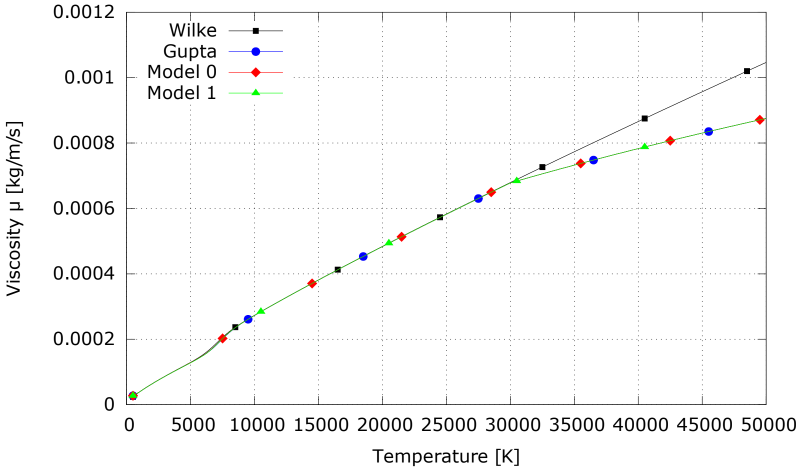

(a) Mixture viscosity coefficient μ

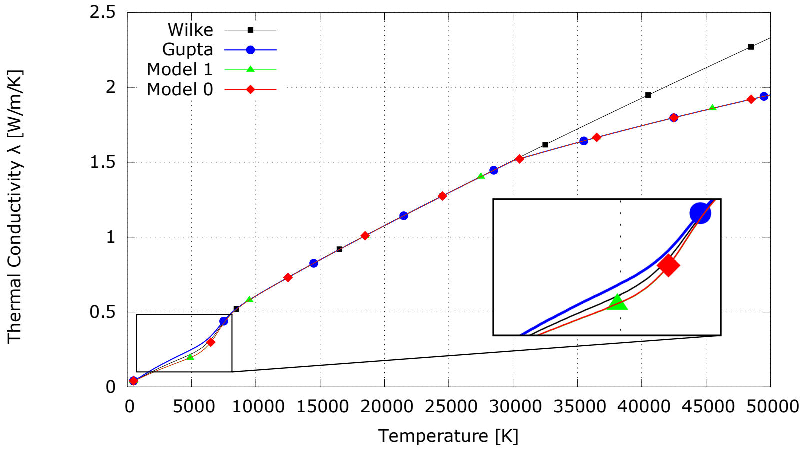

(b) Mixture thermal conductivity coefficient λ

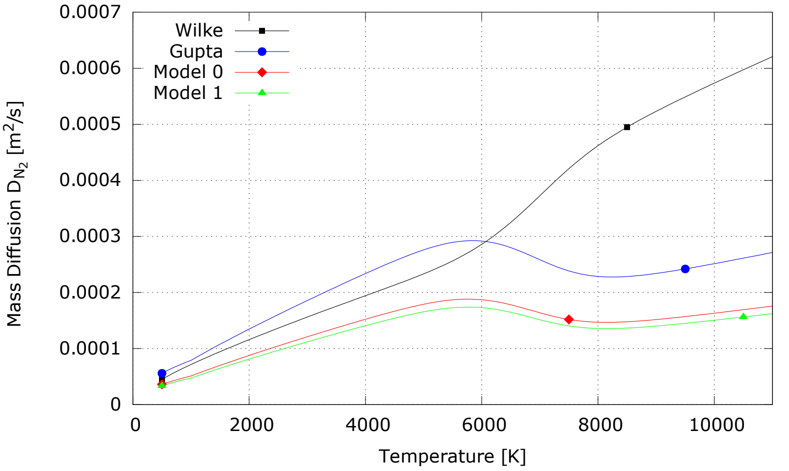

(c) N_2 Mass diffusion coefficient D_{N_2}

Figure 4.2: Comparison of transport models: gas transport properties.

4.1.1 Viscosity

Figure 4.2a shows that, for T $<$ 30,000 K, the value of the mixture viscosity coefficient computed with the four transport models remains approximately the same. However, for T $>$ 30,000 K, the results computed using Wilke's mixing rule begin to deviate significantly from to the other methods. This can be attributed to the fact that Wilke's mixing rule is the only method which does not consider different collision cross-sections in the interactions between particles of different species. Instead, it assumes that all interactions have the same hard-sphere cross-section - which is smaller than the effective average collision cross-sections - yielding a higher viscosity coefficient.

Moreover, Fig. 4.2a shows that, in equilibrium, accounting for state-to-state species in the Gupta's mixing rule for viscosity (Model 0) yields the same results as the corresponding macroscopic mixing rule (Gupta). This is expected given the linearity of the expression for the viscosity coefficient (Eq. 2.34) and given that, under equilibrium conditions, the populations of vibrational energy levels in the state-to-state approach tend to a Boltzmann distribution, which is considered in the Gupta model by definition. Furthermore, it is concluded that the increased cross-section size of $N_2(v)$ vibrational levels (Model 1) may in practice be ignored in the computation of the mixture viscosity coefficient, since it has no impact comparing to Model 0.

4.1.2 Thermal Conductivity

Figure 4.2b shows the global mixture thermal conductivity coefficient calculated with the same four different models. Generally, the obtained results show a similiar behaviour to those obtained for viscosity. For 8,000 $<$ T $<$ 30,000 K, the four methods all compute approximately the same value for thermal conductivity. For T $>$ 30,000 K, results determined by Wilke's mixing rule begin to yield higher a thermal conductivity coefficient comparing to the other methods. Again, this is due to Wilke's assumption that all interactions between any particles present the same (hard sphere) cross-section.

For T $<$ 8,000 K, the Eucken relation (Wilke), Gupta's mixing rule and Model 0 yield slightly different results. This difference is more prominent for temperatures around 6,000 K, which coincides with the temperature for which N_2 and N concentrations equilibrate (see Fig. 4.1).

In order to better understand these differences, the contribution of each thermal energy mode to the N_2 thermal conductivity is plotted in Fig. 4.3. Figure 4.3a compares the Eucken relation (Wilke) to Gupta model, whereas Fig. 4.3b compares Model 0 against Model 1. For these two last models, the contribution of each thermal energy mode to the N_2 thermal conductivity was obtained as the sum of each vibrational level $N_2(v)$ contribution.

Analysing both Figs. 4.3a and 4.3b, the contribution of each thermal energy mode reaches a peak approximately at around T = 6,000 K, for which N_2 and N equilibrate. Moreover, as expected, results tend to zero at T = 11,000 K, since above this temperature the N_2 chemical species is completely dissociated.

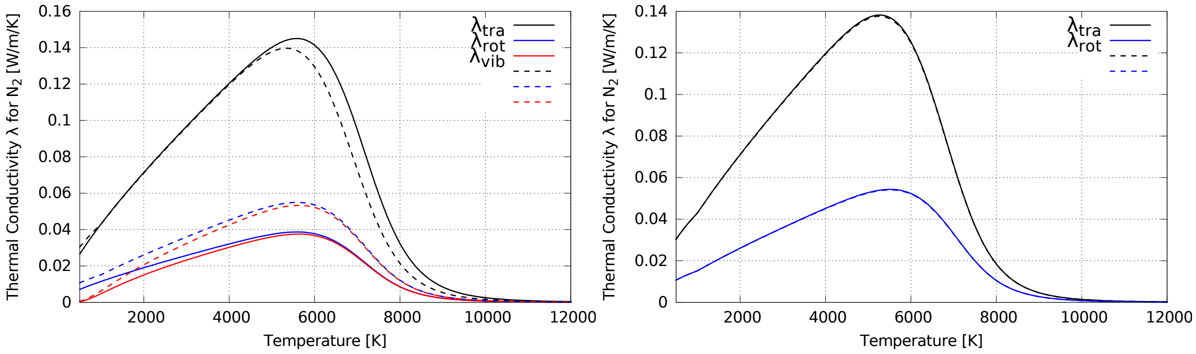

(a) Wilke/Blottner/Eucken vs. Gupta-Yos/CCS macroscopic models.

(b) Model 0 vs. Model 1.

Figure 4.3: Contributions to the N_2 thermal conductivity of the internal degrees of freedom λ_k, equilibrium N_2/N at 101 kPa.

Comparing to the Eucken relation (Wilke), Fig. 4.3a shows that the Gupta-Yos/CCS model yields lower results of the translational contribution for T $>$ 5,000 K and higher results for the rotational and vibrational contributions, for the whole temperature range. These differences are likely due to the over-simplistic assumptions of Wilke's model. Figure 4.3b shows that, similarly to viscosity, thermal conductivity is not affected by the increased size of vibrational levels. Furthermore, for Model 0 and Model 1, the vibrational contribution does not exist, contrary to what happens in Fig. 4.3a. This is consistent with the differences between the consideration of Boltzmann distributions (models Wilke and Gupta) and, alternatively, a state-specific description of the gas (Gupta Model 0 and Model 1). Note that the vibrational thermal conductivity contribution depends on $C_{V,vib} = \frac{\delta \varepsilon_{vib}}{\delta T_{vib}}$ (see Eq. A.21 in Appendix A.3). With a Boltzmann distribution over the vibrational levels, the total vibrational energy is function of the temperature, yielding $C_{V,vib} \neq 0$ and $\lambda_{vib} \neq 0$. On the other hand, in a state-to-state approach, the total vibrational energy is defined as the sum of the energies of each vibrational level which, in turn, depends on the probability of transition between different levels and the type of process ocurring (V-T, V-V-T or V-D – see Section 2.3.1). Since, in this case, the vibrational energy is no longer function of the temperature, we have $C_{V,vib} = 0$ and $\lambda_{vib} = 0$. Furthermore, the electronic contribution does not exist in the four models. Since only 1 electronic level is considered, the concept of distribution does not apply and, again, the electronic energy is not function of the temperature: $C_{V,exc} = 0$ and $\lambda_{exc} = 0$

Focusing again in Fig. 4.2b, up to approximately T = 8,000 K, Gupta's mixing rule yields a slightly higher conductivity than Wilke's mixing rule and both of these results are slightly higher than those provided by Model 0. The decrease in thermal conductivity of Model 0 relative to Gupta's mixing rule is due to the fact that, for N_2, the vibrational contribution for the thermal conductivity vanishes, as explained before. This difference is no longer observable for T $>$ 8,000 K since, in that case, the thermal conductivity coefficient is only due to the concentration of N, for which the contribution to the global coefficient remains the same in the state-to-state and macroscopic description (only the translational contribution is present in both).

For the whole temperature range, one may conclude that, similarly to the case of viscosity, taking into account the increased size of $N_2(v)$ vibrational levels (Model 1) does not impact the mixture thermal conductivity coefficient, since the curves for Model 0 and Model 1 are nearly coincident.

4.1.3 Mass Diffusion

Figure 4.2c shows the mass diffusion coefficient for N_2 for $T < 11{,}000$ K, considering that for $T > 11{,}000$ K N_2 is completely dissociated. For all cases, although the N_2 molar fraction starts decreasing for $T > 6{,}000$ K, D_{N_2} continues to increase, since it does not depend on x_{N_2} (see Eqs. 2.31 and 2.40). For Model 0 and Model 1, D_{N_2} was obtained taking into account the mass diffusion coefficient of each vibrational level $N_2(v)$.

The Wilke model strongly deviates from the others for $T > 6{,}000$ K. This is consistent with the fact that this model does not consider diffusion between particles of different species. As a consequence, diffusion effects are only concentrated in the self-diffusion coefficients, resulting in higher values for D_{N_2}.

Gupta model, Model 0 and Model 1 show a general agreement in behaviour, with a relative maximum occuring at T = 6,000 K, for which N_2 and N concentrations equilibrate. Results provided by the Gupta model yield a significantly higher mass diffusion coefficient than those provided by Model 0 and Model 1. This difference is a consequence of using Gupta's mixing rule - formulated for Boltzmann distributions - to compute the mass diffusion coefficients of vibrational levels. As opposed to the case of viscosity, the expression that provides mass diffusion coefficients is not linear (see Eq. 2.40). Hence, even though equilibrium concentrations are considered, the mass diffusion coefficient of N_2 considering state-specific species does not converge to that of the correspoding chemical species. Moreover, as opposed to the case of viscosity and thermal conductivity, accounting for increased cross-sections of N_2 vibrational levels impacts mass diffusion (Model 1), yielding slightly lower results comparing to Model 0.

4.2 2D Application Case: N_2 Flow Over a Sphere

4.2.1 Impact of Transport Model

Figure 4.4 shows the translational temperature T and the equivalent vibrational temperature T_{vib} for the five test-cases: 1T, 2T, Euler, Model 0 and Model 1. The shock position, indicated by the peak region, is located at, approximately: x = -10.5 mm for Euler, Model 0 and Model 1; x = -9.5 mm for 2T; x = -9mm for 1T. The maximum shock temperatures are, respectively: 21,000 K, 18,000 K, 18,000 K, 17,000 K and 14,000 K.

These differences between shock standoff distances and peak temperature values are expected since, in the state-to-state approach (Euler, Model 0, Model 1), vibrational excitation processes are slower, and the depletion of energy from the translational mode is accordingly slower. The shock layer gas is hotter and therefore less dense. Then the shockwave moves upstream to accomodate this extra volume. For the two-temperature case (2T), VT energy transfer is faster, cooling the shock layer and causing it to move closer to the wall. This is further emphasized in the one-temperature case (1T), for

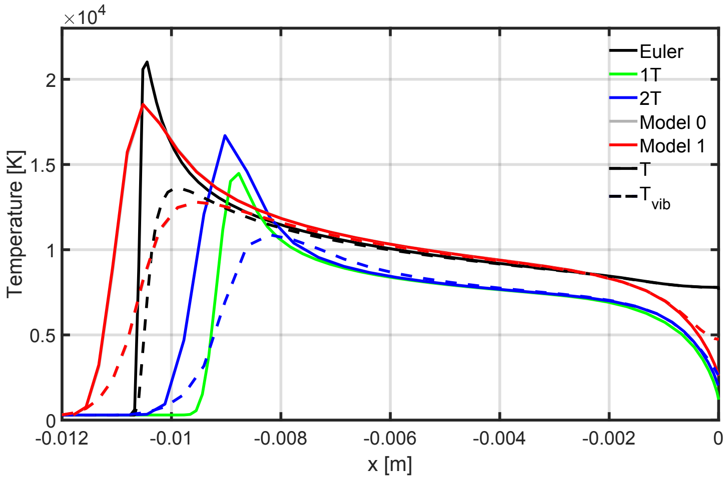

Figure 4.4: Comparison of transport models for T_∞ = 300 K: Stagnation line temperature.

which the VT transfer is essentially instantaneous (since there is T_{tr}–T_{vib} equilibrium) and the shock layer is even cooler.

With regard to the Navier-Stokes state-to-state simulations, there are no differences between Model 0 and Model 1. This is predictable given the results presented in Section 4.1, which have shown that accounting for increased cross-sections of vibrational levels does not impact viscosity and thermal conductivity. Even though for mass diffusion a slight influence was observed, its impact turned out to be completely negligible in a full-scale simulation under the given conditions.

Comparing the sharp shock-layer temperature gradients of the Euler simulation to those resulting from Model 0/Model 1, we see that mass diffusion effects (considerably enchanced by the species gradients from the reactive chemistry behind the bow-shock wave - see Fig. 4.6) significantly even out temperature gradients: the peak temperature value for Model 0/Model 1 is 15% lower than the one predicted in Euler and the shock layer is significantly thicker in the former case. Note that this smaller translational temperature peak has a significant impact on the radiative properties of the flow, which are, on a first approach, T^4 dependent (Planck's black-body law). Radiation source terms in the case of the Navier-Stokes results will be significantly lower than those of the Euler results.

Furthermore, focusing on the results provided by the four viscous simulations (1T, 2T, Model 0, Model 1), the translational and vibrational temperatures tend to equilibrate in the boundary layer, to the same values of the 1T simulation. This is expected since state-to-state and 1T/2T Boltzmann Navier-Stokes models are expected to converge to the same results for the macroscopic conditions that favour a Boltzmann equilibrium – large Damkhohler numbers (which define the ratio of the flow time scale to the chemical time scale). However, this is not completely achieved, especially in the case of Model 0 and Model 1 simulations: the equivalent vibrational temperature T_{vib} starts to deviate from the remaining curves approximately at x = -0.5 mm, and at x = 0 mm T_{vib} is 30% higher than T. This may be explained by insufficient mesh refinement near the wall, or the solution not having advanced enough in time[1]. Quantitatively speaking, comparing to Model 0/Model 1, the temperature at x = 0 mm is about 50% lower for 1T and 40% lower for 2T, which results in a higher wall convective heat flux for the Navier-

---

[1] as implicit simulations would typically crash when attempts at raising the CFL beyond typical values around 0.01 were made

Stokes state-to-state simulations.

In the case of the Euler simulation, refinement in the boundary layer is not essential since the wall is, by definition, adiabatic - which translates in the absence of temperature gradients typically found in a boundary layer. Accordingly, the two temperatures T and T$_{vib}$ start to perfectly converge at x = -4 mm.

Figure 4.5 presents the vibrational distribution functions of N$_2(v)$ vibrational levels. The corresponding mass fractions are normalized by the N$_2$ total mass fraction. Results provided by Model 1 are compared against those provided by Model 0 (Figs. 4.5a, 4.5b, 4.5c) which, in turn, are compared against the Euler simulation (Fig. 4.5d). No results are presented for multi-temperature simulations since, by definition, the populations of vibrational energy levels follow Boltzmann distributions (straight lines in a logarithmic graph).

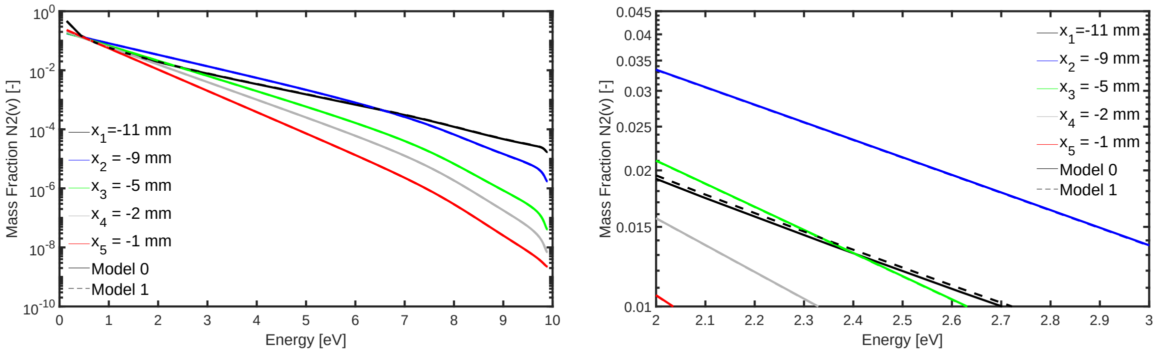

(a) Model 0 vs. Model 1.

(b) Model 0 vs. Model 1 zoom I.

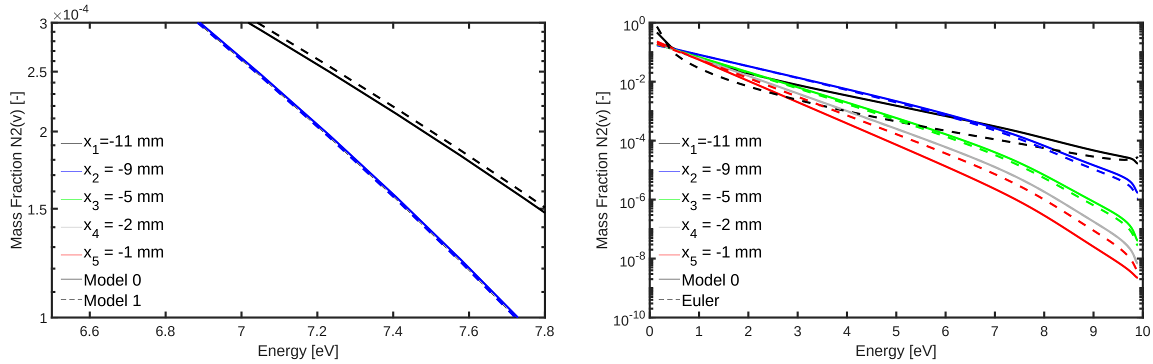

(c) Model 0 vs. Model 1 zoom II.

(d) Model 0 vs. Euler

Figure 4.5: Comparison of transport models for T$_\infty$ = 300 K: vibrational distribution functions of N$_2(v)$ for different positions along the stagnation line.

Generally, these four figures show that, as the distance to the wall decreases and the flow dissociates - the molar fractions of N gradually increase up to 99%, at the expense of the N$_2(v)$ molar fractions -, the curves fall down in the scale.

Figure 4.5a shows that differences between Model 0 and Model 1 are vanishingly small. Considering that near-dissociative levels have significantly higher internuclear distances (see Table B.1), it is postulated that dissociation-recombination reactions are dominant over any mass diffusion processes that might be enchanced by these increased collisional cross-sections. In the shockwave region (x = -11mm), where the large concentration gradients enchance mass diffusion, the differences between Model 0 and Model 1 are more apparent, for lower and higher energy levels (see Figs. 4.5b and 4.5c). Right after the peak region (x = -9 mm), slight differences between the two models can still be observed for higher energy levels, since the cross-sections of these levels will be more enhanced than those of the low-lying ones (see Table B.1). However, differences between Model 0 and Model 1 are small enough to conclude that increased collisional cross-sections for vibrational levels may in practice be ignored.

In the boundary layer region (x = -1 mm) the flow time scales increase significantly due to a decrease in velocity and, consequently, a Boltzmann equilibrium is nearly reached, as dissociation and recombination processes tend to equilibrate.

Moreover, in Fig. 4.5d, distributions provided by Model 0 are compared with those provided by the Euler simulation (since Model 1 yields approximately the same distributions as Model 0, the corresponding results are not explicitly compared to the Euler simulation). For x = -11 mm, x = -9 mm and x = -5 mm, mass fractions of the Euler simulation are lower than those of Model 0, which can be attributed to more abrupt dissociation due to absence of transport phenomema and, consequently, a higher temperature peak. As for x = -1 mm, due to the absence of a boundary layer and consequent higher temperatures in the Euler case, recombination reactions do not occur, nor does equilibration (that would be translated into a straight line - Boltzmann distribution). However, these higher temperatures favour vibrational excitation, which is demonstrated by the higher concentrations of vibrational levels, compared to Model 0.

Figure 4.6 presents the mole fractions of chemical species N_2 and N. Apart from the boundary layer region, the obtained curves show a similar behaviour. In the upstream region only N_2 molar fractions are found. As soon as the temperature rises - which happens for different positions in the stagnation line depending on the simulation to be considered - dissociation reactions begin to occur, causing the molar fractions of atomic nitrogen to gradually increase and, naturally, the ones of molecular nitrogen to decrease. With respect to Model 0 and Model 1, once again the impact of the latter turns out to be completely negligible (coincident curves).

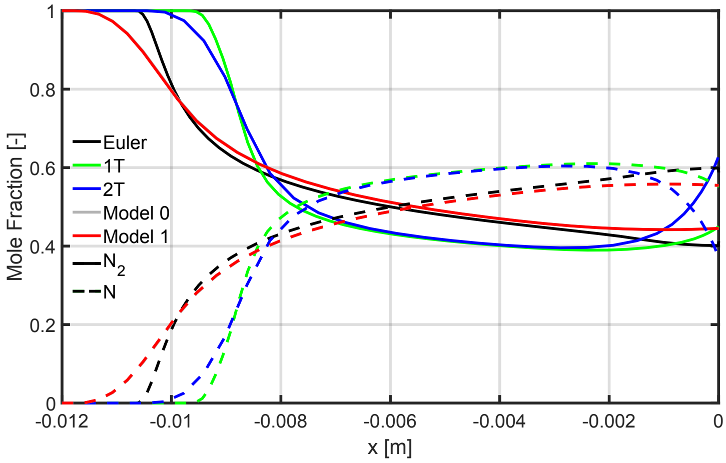

Figure 4.6: Comparison of transport models for T_∞ = 300 K: Stagnation line mole fractions of chemical species N_2 and N.

Analysing the region where dissociation starts to occur, there are some noteworthy differences between the different models. In the case of viscous simulations, reactions initiate at x = -11.5 mm for Model 0 and Model 1, at x = -10.5 mm for 2T and, lastly, at x = -10 mm for 1T. This is consistent with the different shock positions associated with each simulation (see Fig. 4.4), which is expected since dissociation reactions are activated by the corresponding high-temperatures. Comparing the Euler state-to-state simulation to the Navier-Stokes state-to-state simulations (Model 0 and Model 1), the only difference is the enhanced smoothness in the latter case, explained by the presence of mass diffusion processes.

Focusing on the boundary layer region, recombination effects are clearly noticeable in the case of both multi-temperature simulations (denoted by the increase/decrease in the molar fractions of N_2/N). This phenomenon is more enhanced in the case of the 2T simulation, for which the N_2 molar fraction is 30% higher than for 1T, contrary to what was expected. Analysing Fig. 4.1, it is concluded that, in equilibrium conditions, N_2 concentrations are smaller for higher temperatures. In the full-scale simulation, at x = 0 mm, temperatures provided by the 2T simulation are higher than those of the 1T case (see Fig. 4.4) and, accordingly, recombination should be more pronounced in this latter case. A probable justification for this contradiction is the fact that equilibrium is not completely achieved near the surface of the vehicle, likely due to poor refinement in this region, as explained before.

In the case of state-to-state simulations, there are no recombination reactions near the wall for the inviscid results since, in this case, there is no decrease in temperature given the adiabatic boundary condition. For Model 0/Model 1, there are very slight recombination effects near the surface of the vehicle. This is not obvious when observing the graph, once again because the new state of equilibrium is not properly captured by the mesh. However, this was verified through analysis of the output data. At x = 0 mm, there is about 10% more N_2 for Model 0 than for Euler. This difference is due to mass diffusion effects, since recombination is negligible in Model 0.

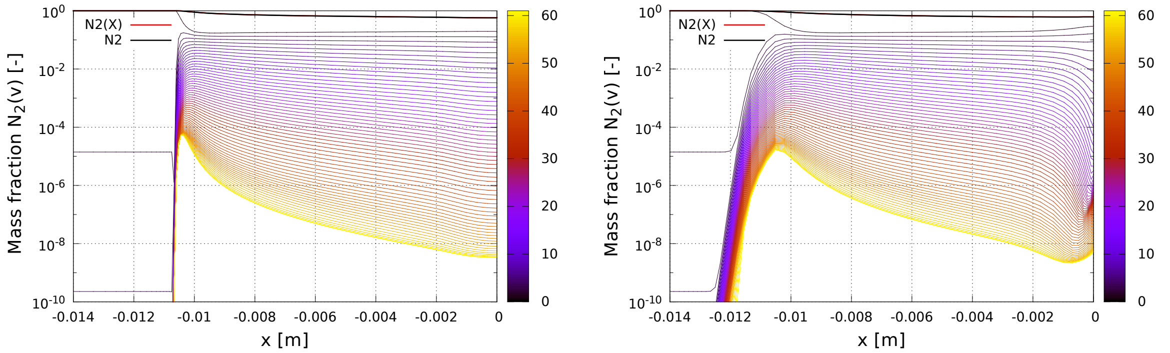

(a) Model 0.

(b) Euler.

Figure 4.7: Comparison between Euler (left) and Navier-Stokes (right) state-to-state simulations for T_∞ = 300K: mass fractions of $N_2(v)$ vibrational levels along the stagnation line.

Figure 4.7 presents the mass fraction of each vibrational level along the stagnation line, for both the Euler and Model 0 simulations. For each case, right before the temperature peak region, there is a significant increase in the population of all the upper vibrational levels of N_2, at the expense of the v = 0 level, caused by the high increase in temperature encountered in the shock wave. Shortly after the temperature peak, around x = -10.5 mm, dissociation of N_2 takes over and all the energy levels start being depleted more or less evenly. This means that multiquantum transitions between different levels are as dominant as monoquantum transitions.

Comparing both figures, the mass diffusion effects present in Model 0 are evident. This is clear along the entire stagnation line, where the curves resulting from Model 0 are much smoother than those resulting from Euler. Furthermore, around x = -1 mm, we see a drastic increase of the population of higher $N_2(v)$ levels, in Model 0. This occurs because the flow reaches the boundary layer with about a 55% degree of dissociation, and the sudden temperature decrease in the boundary layer will lead to a strongly recombining flow, favouring recombination in the upper levels. On the other hand, for the Euler simulation no gradients are observed in x = 0 mm, which, once again, is explained by the absence of a boundary layer.

Figures 4.8 show the temperature field: Euler (top left) vs. Model 0 (bottom left) and 2T (top right) vs. Model 0 (bottom right).

Comparing Euler to Model 0 (Fig. 4.8; left side), it is verified that the shock standoff distance does not change, however the shock layer thickness increases significantly in the latter case. Moreover, one can confirm that a boundary layer exists along the whole surface of the sphere (dark line along the surface), which does not happen in the Euler simulation. The presence of the boundary layer is also perceptible in the results provided by the two-temperature simulation. Comparing these results to those provided by Model 0 (Fig. 4.8; right side), there are two main differences. The shock layer is significantly thicker for Model 0, not only in the stagnation line but also along the sphere's surface. Furthermore, the shock standoff distance is larger for the state-to-state simulation (which had already been observed in Fig. 4.4).

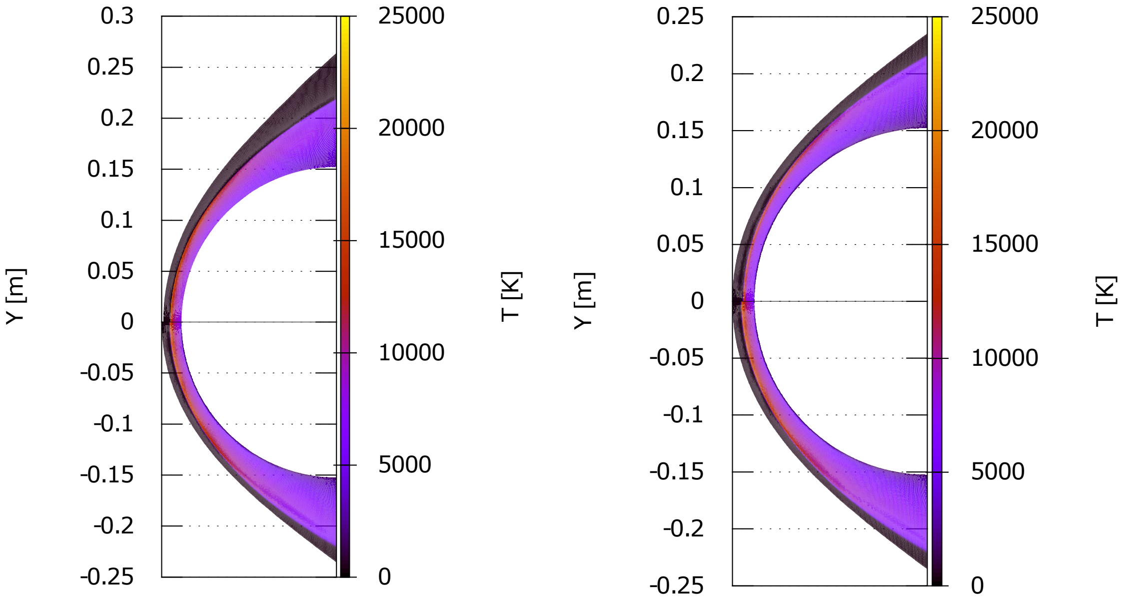

Figure 4.8: Temperature field for T$_\infty$ = 300 K: Euler (top left) vs. Model 0 (bottom left), and 2T (top right) vs. Model 0 (bottom right).

4.2.2 Impact of Freestream Temperature

An addtional set of simulations has been carried out considering a freestream temperature of 700 K. Figure 4.9 shows the stagnation line temperature of Model 0 and Model 1 for T$_\infty$ = 700 K and of Model 0 for T$_\infty$ = 300 K.

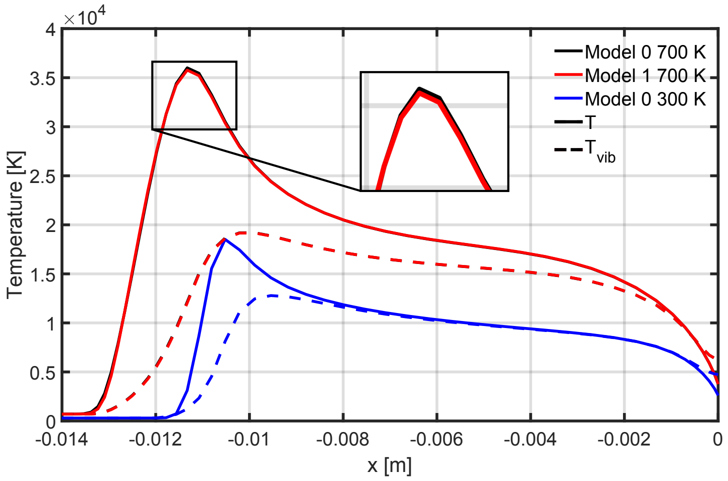

Figure 4.9: Impact of the freestream temperature: Stagnation line temperature for Model 0 and Model 1 at T$_\infty$ = 700 K and for Model 0 at T$_\infty$ = 300 K.

Comparing results provided by the different freestream temperatures, generally a similar behaviour is observed. The shock standoff distance is about 10% larger for T$_\infty$ = 700 K. Also for this case, the peak temperature value is about 50% higher than for T$_\infty$ = 300 K. These two main differences are explained by the fact that higher freestream velocities (a consequence of a higher freestream temperature, since $V_\infty = M_\infty \times \sqrt{\gamma R T_\infty}$) leads to a more energetic flow.

Additionally, for T_∞ = 700 K the curve for the translational temperature is moderatly smoother in the peak region, where temperature gradients are larger. This is indicative of a more adequate mesh refinement in the shock-layer than for the case of T_∞ = 300 K.

Furthermore, for T_∞ = 700 K, the impact of accounting for increased cross-sections of vibrational levels (Model 1) is negligible, similarly to what was concluded for For T_∞ = 300 K. However, zooming in the peak temperature for T_∞ = 700 K, it is slightly higher for Model 0 than for Model 1, while for T_∞ = 300 K both curves were coincident along the whole stagnation line (see Fig. 4.4). This may be attributed to two factors: (a) better mesh refinement for T_∞ = 700 K; (b) since, for T_∞ = 700 K, temperatures reach much higher values, the corresponding gradients will be larger and diffusion phenomena will be enhanced. Accounting for larger effective cross-sections (Model 1) results in a slightly more diffusive flow, as compared to Model 0. This is an unexpected outcome, since Model 1 yielded lower mass diffusion coefficients than Model 0 in the analysis conducted in Section 4.1.3 (see Fig. 4.2a). However, this analysis did not take into account the influence of pressure, which may explain this apparent contradiction. Future work should include a parametric study on the evolution of transport coefficients with pressure, using Model 1.

Nevertheless, for T_∞ = 700 K, refinement in the boundary layer region is still insufficient. Similarly to the case of T_∞ = 300 K, equilibrium is not achieved near the sphere's surface, since results of T_{vib} deviate from those of T for about 25% in the case of T_∞ = 700 K, at x = 0 mm. Moreover, for T_∞ = 700 K, the translational temperature is 30% higher than for T_∞ = 300 K at the wall, resulting in a higher convective heat flux, which is consistent with the fact that the flow is more energetic in the former case.

Figure 4.10 shows the vibrational distribution functions of $N_2(v)$ for different positions along the stagnation line. Mass fractions of vibrational levels $N_2(v)$ are normalized by the N_2 mass fraction. Figure 4.10a compares Model 0 to Model 1 at T_∞ = 700 K (left), while Fig. 4.10b compares T_∞ = 700 K to T_∞ = 300 K for Model 0 (right).

Analysing Fig. 4.10a, similarly to the case of T_∞ = 300 K (see Fig. 4.5a), it is concluded that: (a) the increased cross-sections of vibrational levels considered in Model 1 have no impact in the vibrational distribution functions of $N_2(v)$, comparing to Model 0 (b) a Boltzmann distribution is nearly reached close to the wall.

Focusing on the comparison between different freestream temperatures (Fig. 4.10b), as the distance from the wall decreases, concentrations of vibrational levels are increasingly higher for more energetic levels, in the case of T_∞ = 700 K. This is expected, since higher temperatures favour molecular vibrational excitation.

The impact of freestream temperature on stagnation line mole fractions of chemical species is studied in Fig. 4.11. Model 0 is compared to Model 1 for T_∞ = 700 K and T_∞ = 700 K is compared to T_∞ = 300 K for Model 0.

For T_∞ = 700 K, there are no differences between Model 0 and Model 1, which is expected given the results presented in the previous two figures. Analysing the impact of the freestream temperature for Model 0, there are considerable differences between the two cases. For T_∞ = 700 K, dissociation

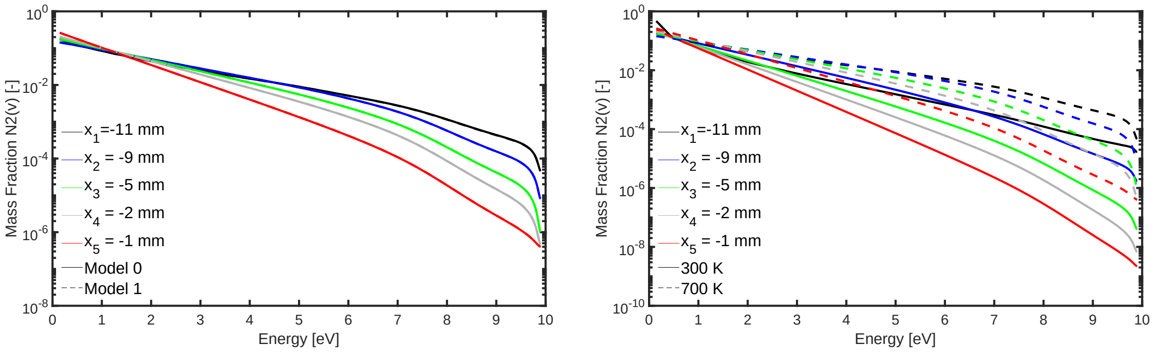

(a) Model 0 vs. Model 1 at T_∞ = 700 K.

(b) T_∞ = 700 K vs. T_∞ = 300 K for Model 0.

Figure 4.10: Vibrational distribution functions of $N_2(v)$ for different positions along the stagnation line.

reactions start occurring sooner - around x = -13 mm for T_∞ = 700 K and x = -12 mm for T_∞ = 300 K -, which is consistent with the corresponding shock standoff distances. Moreover, dissociation effects are significantly more enhanced for T_∞ = 700 K - approximately 99% of atomic nitrogen at the wall for T_∞ = 700 K against 55% for T_∞ = 300 K. This is expected since higher temperatures tend to favour dissociation.

Nonetheless, in the boundary layer region, recombination effects are almost nonexistent. As observed in Fig. 4.9, equilibrium conditions are not reached near the wall, probably for not being captured by the mesh.

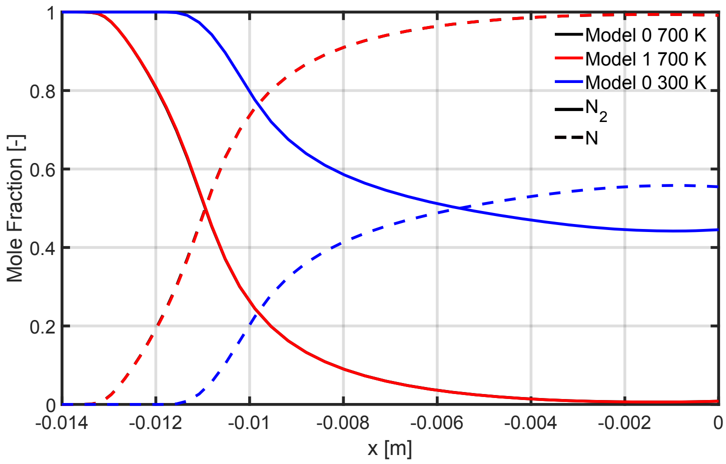

Figure 4.11: Impact of freestream temperature: stagnation line mole fractions of chemical species N_2 and N - Model 0 vs. Model 1 for T_∞ = 700 K and T_∞ = 700 K vs. T_∞ = 300 K for Model 0.

Finally, Fig. 4.12, shows the temperature field for Model 0, comparing results obtained with T_∞ = 700 K (top) against those obtained with T_∞ = 300 K (bottom). The higher temperature values resulting from having T_∞ = 700 K are evident in the entire flowfield. Moreover, results obtained for this simulation show a slightly larger shock standoff distance, which had already been observed in the stagnation line temperature plot (Fig. 4.9). The most visible difference between the two temperatures fields is the shock layer thickness, which is considerably larger for the case of T_∞ = 700 K, along the whole surface of the sphere. This is caused by the corresponding higher peak temperature and consequent larger temperature gradients, from which stronger mass diffusion effects result.

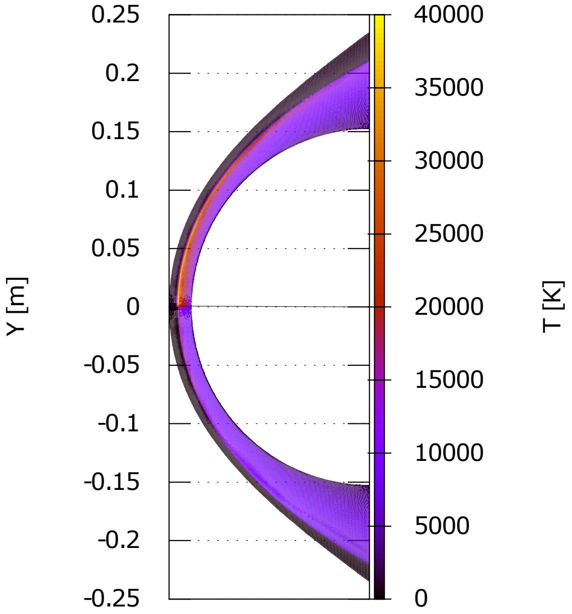

Figure 4.12: Impact of freestream temperature: temperature field - T_∞ = 700 K (top) vs. T_∞ = 300 K (bottom) for Model 0.

Chapter 5

Conclusions

5.1 Achievements

This thesis has provided a better understanding of the flowfield experienced by a space vehicle during reentry into Earth. High-speed reentry is characterized by strong nonequilibrium conditions, under which state-to-state vibrational kinetics was found to significantly impact the transport properties of the gas.

In light of this, a successfull full state-to-state Navier-Stokes simulation was performed for a nitrogen flow over a sphere. In order to account for transport phenomena and non-Boltzmann distributions over the vibrational levels, two simplified state-specific transport models were employed. Model 0 was formulated as a direct adaptation of the macroscopic Gupta-Yos/CCS model to state-to-state species. The more detailed Model 1 followed the same formulation, also accounting for the increased cross-sections of vibrationally excited molcules in the collision terms. For comparison purposes, multi-temperature Navier-Stokes and Euler state-to-state simulations were also performed.

As expected, a comparison between multi-temperature and state-to-state approaches resulted in a significantly more energetic flow for the latter case, translated into larger shock standoff distances and higher peak temperatures (respectively, 10% and 5% larger than for the two-temperature case). However, results provided by the state-to-state Navier-Stokes simulations did not converge to values identical to those provided by multi-temperature simulations at the wall, where equilibrium conditions are expected to be encountered. It was concluded that, in order to capture the steep gradients occuring in the boundary layer, more rigorous mesh refinement is necessary in this region.

Simulations using state-specific transport coefficients resulted in smoother variations of the flow properties comparing to the Euler case: a significantly thicker shock-layer and a 15% lower peak temperature. A comparison between Model 0 and Model 1 allowed confirming that the coupled effect of vibrational molecular size and non-Boltzmann distributions on the transport properties is negligible and does not impact the flowfield.

The impact of the freestream temperature (translated into freestream velocity) was evaluated for 300 and 700 K (7 and 10.7 km/s for the same Mach number, respectively). For the higher freestream temperature, the effects of microscopic thermochemical processes such as dissociation and vibrational excitation are emphasised. Moreover, there is a slight influence of the cross-section effective size in the peak temperature, but is still considered to be negligible.

These findings may have a non-negligible impact on the design of TPS systems for very high speed entries (above 10km/s), since they particularly provide a more faithful description of the flow properties in the shock-layer, which is critical to the determination of radiative heat fluxes. Different shock-standoff values may also impact convective heat fluxes, in case the shock layer tends to mix with the boundary layer, in the absence of a quasi-steady state intermediary zone.

5.2 Future Work

The results obtained in this thesis lay the groundwork for further research. The next step would be the inclusion of a detailed state-specific transport model in the governing fluid dynamic equations, such as the one proposed by Kustova. A more accurate prediction of the properties of a hypersonic flow under strong nonequlibrium conditions, rather than using simplified models, would require the determination of the transport coefficents on the basis of the state-to-state kinetic theory.

In the specific case of this study, a higher level of accuracy should be achieved in the boundary layer region, by means of improving the mesh refinement in this region. This would allow clarifying a few discrepancies that were found in the boundary layer region when comparing the different macrsocopic and state-to-state models, and specifically determining if these are physical in nature or merely the result of an insufficiently converged solution (in terms of mesh and computation time).

Bibliography

[1] P. Desai, D. Lyons, J. Tooley, and J. Kangas. Entry, descent, and landing operations analysis for the stardust entry capsule. *Journal of Spacecraft and Rockets*, 45(6):1262–1268, 2008.

[2] J. J. Bertin. *Hypersonic Aerothermodynamics*. AIAA, 1994.

[3] D. F. Potter. *Modelling of radiating shock layers for atmospheric entry at Earth and Mars*. PhD thesis, The University of Queensland, Australia, 2011.

[4] S. Chapman and T. G. Cowling. *The mathematical theory of non-uniform gases*. Cambridge University Press, 1964.

[5] J. Clarke and M. McChesney. *The dynamics of real gases*. Washington,DC: Butterworth Inc., 1964.

[6] E. Josyula, W. F. Bailey, and C. J. Suchyta. Dissociation modeling in hypersonic flows using state-to-state kinetics. *Journal of Thermophysics and Heat Transfer*, 25(1):34–47, 2011.

[7] J. Hao, J. Wangb, and C. Leea. Assessment of vibration–dissociation coupling models for hypersonic nonequilibrium simulations. *Aerospace Science and Technology*, 67:433–442, 2017.

[8] E. Josyula, A. Aliat, and P. Vedula. Multiquantum state-to-state transitions in hypersonic blunt body flows. AIAA Paper 2011-532, 2011.

[9] H. S. Massimia, H. Shen, C. Y. Wen, Y. S. Chen, and S. M. Liang. Numerical analysis of hypersonic flows around blunt-nosed models and a space vehicle. *Aerospace Science and Technology*, 43: 360–371, 2015.

[10] F. Bonelli, M. Tuttafesta, G. Colonna, L. Cutrone, and G. Pascazio. An mpi-cuda approach for hypersonic flows with detailed state-to-state air kinetics using a gpu cluster. *Computer Physics Communications*, 219:178–195, 2017.

[11] J. G. Kim and I. D. Boyd. State-resolved master equation analysis of thermochemical nonequilibrium of nitrogen. *Chemical Physics*, 415:237–246, 2013.

[12] B. Lopez and M. Lino da Silva. Spark: A software package for aerodynamics, radiation and kinetics. AIAA Paper 2016-4025, 2016.

[13] G. Sarma. Physico–chemical modelling in hypersonic flow simulation. *Progress in Aerospace Sciences*, 36:281–349, 2000.

[14] H. G. Hornung. Non-equilibrium dissociating nitrogen flow over spheres and circular cylinders. *Journal of Fluid Mechanics*, 53:149–176, 1972.

[15] C. Y. Wen and H. G. Hornung. Non-equilibrium dissociating flow over spheres. *Journal of Fluid Mechanics*, 299:389–405, 1995.

[16] G. S. Deiwert and G. Eitelberg. Real gas/blunt cone phase II report. *Hypersonic experimental and computational capability, improvement, and validation*, AGARD-AR-319(II), 1998.

[17] M. Holden. Shock interaction phenomena in hypersonic flows. AIAA Paper 98-2751, 1998.

[18] J. Muylaert, L. Walpot, M. Spel, P. Sagnier, K. Hannemann, and H. Olivier. A review of european code validation studies in high enthalpy flow. AIAA Paper 98-2769, 1998.

[19] L. C. Scalabrin and I. D. Boyd. Numerical simulations of the FIRE-II convective and radiative heating rates. AIAA Paper 2007-4044, 2007.

[20] J. Hao, J. Wang, and C. Lee. Numerical study of hypersonic flows over reentry configurations with different chemical nonequilibrium models. *Acta Astronautica*, 126:1–10, 2016.

[21] J. Hao, J. Wangb, Z. Gaoa, C. Jianga, and C. Leea. Comparison of transport properties models for numerical simulations of mars entry vehicles. *Acta Astronautica*, 130:24–33, 2017.

[22] C. R. Wilke. A viscosity equation for gas mixtures. *The Journal of Chemical Physics*, 18(4):517–519, 1950.

[23] P. Gnoffo, R. N. Gupta, and J. L. Shinn. Conservation equations and physical models for hypersonic air flows in thermal and chemical nonequilibrium. Technical report, NASA, 1989.

[24] G. V. Candler, J. Olejniczak, and B. Harrold. Detailed simulation of nitrogen dissociation in stagnation regions. *Physics of Fluids*, 9:2108–2117, 1997.

[25] E. Josyula and W. F. Bailey. Vibration–dissociation coupling using master equations in nonequilibrium hypersonic blunt-body flow. *Journal of Thermophysics and Heat Transfer*, 15(2):157–167, 2001.

[26] E. V. Kustova and G. M. Kremer. Chemical reaction rates and non-equilibrium pressure of reacting gas mixtures in the state-to-state approach. *Chemical Physics*, 445:82–94, 2014.

[27] E. Nagnibeda. The structure of the relaxation zone behind shock waves in the reacting gas flows. Aerothermodynamics for Space Vehicles, ESA SP 367, ESA Publication Division, ESTEC, Noordwijk, The Netherlands, pp. 299–303, 1995.

[28] F. Lordet, J. Meolans, A. Chauvin, and R. Brun. Nonequilibrium vibration-dissociation phenomena behind a propagating shock wave: Vibrational population calculation. *Shock Waves*, 4:299–312, 1995.

[29] I. Adamovich, S. Macheret, J. Rich, and C. Treanor. Vibrational energy transfer rates using a forced harmonic oscillator model. *Journal of Thermophysics and Heat Transfer*, 12(1):57–65, 1998.

[30] S. Ruffin and C. Park. Vibrational relaxation of anharmonic oscillators in expanding flows. AIAA Paper 92–0806, 1992.

[31] G. Colonna, M. Capitelli, M. Tuttafesta, and D. Giordano. Non-arrhenius no formation rate in one-dimensional nozzle airflow. *Journal of Thermophysics and Heat Transfer*, 13(3):372–375, 1999.

[32] I. Armenise, M. Capitelli, G. Colonna, and C. Gorse. Nonequilibrium vibrational kinetics in the boundary layer of re-entering bodies. *Journal of Thermophysics and Heat Transfer*, 10(3):397–405, 1996.

[33] B. Lopez, M. Lino da Silva, V. Guerra, and J. Loureiro. Coupled hydrodynamic/state- specific high-temperature modeling of nitrogen vibrational excitation and dissociation. *Journal of Thermophysics and Heat Transfer*, AIAA Paper 2013-1585484, 2013.

[34] E. Josyula, W. F. Bailey, and K. Xu. Nonequilibrium relaxation in high speed flows. AIAA Paper 2004-2468, 2004.

[35] E. Josyula, J. M. Burt, and K. Xu. Influence of thermochemical nonequilibrium on transport properties for hypersonic flow simulations. AIAA Paper 2012-3191, 2012.

[36] E. Josyula, J. M. Burt, E. Kustova, and M. Mekhonoshina. State-to-state kinetic modeling of dissociating and radiating hypersonic flows. AIAA Paper 2015-0475, 2015.

[37] E. Josyula, J. M. Burt, E. Kustova, and P. Vedula. Influence of state-to-state transport coefficients on surface heat transfer in hypersonic flows. AIAA Paper 2014-0864, 2014.

[38] H. Struchtrup and P. Taheri. Macroscopic transport models for rarefied gas flows: a brief review. *IMA Journal of Applied Mathematics*, 16:672–697, 2011.

[39] E. V. Kustova and E. A. Nagnibeda. Transport properties of a reacting gas mixture with strong vibrational and chemical nonequilibrium. *Chemical Physics*, 233:57–75, 1998.

[40] K. Sutton and P. A. Gnoffo. Multi-component diffusion with application to computational aerothermodynamics. AIAA Paper 98-2575, 1998.

[41] G. E. Palmer and M. J. Wright. Comparison of methods to compute high-temperature gas viscosity. *Journal of Thermophysics and Heat Transfer*, 17(2):232–239, 2003.

[42] Y. Chen and F. S. Milos. Finite-rate ablation boundary conditions for a carbon-phenolic heat-shield. AIAA Paper 2004-2270, 2004.

[43] T. E. Magin and G. Degrez. Transport algorithms for partially ionized and unmagnetized plasmas. *Journal of Computational Physics*, 198(2):424–449, 2004.

[44] R. Gosse and G. Candler. Diffusion flux modeling: Application to direct entry problems. AIAA Paper 2005-389, 2005.

[45] H. Alkandry, I. D. Boyd, and A. Martin. Comparison of models for mixture transport properties for numerical simulations of ablative heat-shields. AIAA 2013-0303, 2013.

[46] B. F. Armaly and L. Sutton. Viscosity of multicomponent partially ionized gas mixtures. AIAA Paper 80-1495, 1980.

[47] M. Wright, D. Bose, and G. V. Candler. Data-parallel line relaxation method for the navier-stokes equations. *AIAA Journal*, 36(9):1603–1609, 1998.

[48] J. D. Ramshaw and C. H. Chang. Friction weighted self-consistent effective binary diffusion approximation. *Journal of Non-Equilibrium Thermodynamics*, 21:223–232, 1996.

[49] J. D. Ramshaw and C. H. Chang. Ambipolar diffusion in two-temperature multicomponent plasmas. *Plasma Chemistry and Plasma Processing*, 13(3):489–498, 1993.

[50] K. Sutton and P. A. Gnoffo. Multi-component diffusion with aerothermodynamics. AIAA 98-2575, 1998.

[51] E. Nagnibeda and E. Kustova. *Nonequilibrium Reacting Gas Flows. Kinetic Theory of Transport and Relaxation Processes*. Springer-Verlag, Berlin, 2009.

[52] D. Bruno, M. Capitelli, E. Kustova, and E. Nagnibeda. Non-equilibrium vibrational distributions and transport coefficients of $N_2(v)$/–N mixtures. *Chemical Physics Letters*, 308:463–472, 1999.

[53] O. Kunova, E. V. Kustova, M. Mekhonoshina, and E. Nagnibeda. The influence of state-to-state kinetics on diffusion and heat transfer behind shock waves. AIP Conference Proceedings 1628, 1202 (2014).

[54] O. Kunova, E. V. Kustova, M. Mekhonoshina, and E. Nagnibeda. Non-equilibrium kinetics, diffusion and heat transfer in shock heated flows of N_2/N and O_2/O mixtures. *Chemical Physics*, 463:70–81, 2015.

[55] I. Armenise, M. Capitelli, E. Kustova, and E. Nagnibeda. Influence of nonequilibrium kinetics on heat transfer and diffusion near re-entering body. *Journal of Thermophysics and Heat Transfer*, 13 (2):210–218, 1999.

[56] I. Armenise, M. Barbato, M. Capitelli, and E. Kustova. State-to-state catalytic models, kinetics, and transport in hypersonic boundary layers. *Journal of Thermophysics and Heat Transfer*, 20(3): 465–476, 2006.

[57] M. Capitelli, I. Armenise, and C. Gorse. State-to-state approach in the kinetics of air components under re-entry conditions. *Journal of Thermophysics and Heat Transfer*, 11(4):570–578, 1997.

[58] E. Kustova and G. M. Kremer. Influence of state-to-state vibrational distributions on transport coefficients of a single gas. AIP Conference Proceedings 1786, 070002 (2016).

[59] E. Kustova and G. M. Kremer. Effect of molecular diameters on state-to-state transport properties: The shear viscosity coefficient. *Chemical Physics Letters*, 636:84–89, 2015.

[60] B. Lopez. *Simulation des Ecoulements de Plasma Hypersonique Hors Equilibre Thermochimique*. PhD thesis, Université D'Orléans, France, 2010.

[61] J. D. Anderson. *Hypersonic and High Temperature Gas Dynamics*. AIAA, 2nd edition, 1989.

[62] C. Park. Rotational relaxation of n_2 behind a strong shock wave. *Journal of Thermophysics and Heat Transfer*, 18(4):527–533, 2004.

[63] M. Lino da Silva, J. Loureiro, and V. Guerra. Rotational nonequilibrium in state-resolved models for shock-heated flows. *Chemical Physics*, 398:96–103, 2012.

[64] M. Lino da Silva, J. Loureiro, and V. Guerra. Nonequilibrium dissociation and recombination rates in nitrogen: From shock waves to discharge conditions. *Chemical Physics*, 358(1-2):123–131, 2009.

[65] M. Lino da Silva, V. Guerra, and J. Loureiro. A review of non-equilibrium dissociation rates and models for atmospheric entry studies. *Plasma Sources Science and Technology*, 18:1–11, 2009.

[66] B. Lopez, M. Lino da Silva, V. Guerra, and J. Loureiro. Coupled hydrodynamic/state-specific high-temperature modeling of nitrogen vibrational excitation and dissociation. AIAA Paper 2013-1585484, 2013.

[67] R. C. Millikan and D. R. White. Systematics of vibrational relaxation. *The Journal of Chemical Physics*, 39:3209–3213, 1963.

[68] S. A. Losev, P. V. Kozlov, L. A. Kuznetsova, V. N. Makarov, and Y. V. Romanenko. Radiation of a mixture CO_2-N_2-ar in shock waves: Experiment and modelling. *Aerothermodynamics for Space Vehicles*, 426, 1998.

[69] E. Josyula, J. M. Burt, W. F. Bailey, and P. Vedula. Role of state-to-state kinetics in determination of transport coefficients for hypersonic flow simulations. *The Open Plasma Physics Journal*, pages 173–180.

[70] F. G. Blottner, M. Johnson, and M. Ellis. Chemically reacting viscous flow program for multi- component gas mixtures. Technical report, Sandia Laboratories, 1971.

[71] W. G. Vincenti and C. H. Kruger. *Introduction to Physical Gas Dynamics*. Krieger Publishing Company, 2002.

[72] R. N. Gupta, J. M. Yos, and R. A. Thompson. A review of reaction rates and thermodynamic and transport properties for the 11-species air model for chemical and thermal nonequilibrium calculations to 30000 k. Technical report, NASA, 1990.

[73] R. A. Svehla. Estimated viscosities and thermal conductivities of gases at high temperatures. Technical report, NASA, 1962.

[74] M. Lino da Silva, V. Guerra, and J. Loureiro. State-resolved dissociation rates for extremely nonequilibrium atmospheric entries. *Journal of Thermophysics and Heat Transfer*, 21(1):40–49, 2007.

[75] M. Capitelli, G. Cologna, and F. Esposito. On the coupling of vibrational relaxation with the dissociation-recombination kinetics: From dynamics to aerospace applications. *Journal of Physical Chemistry A*, 108(41):8930–8934, 2004.

[76] B. Lopez, M. Lino da Silva, V. Guerra, and J. Loureiro. Vibrational distributions in n2 with an improved calculation of energy levels using the rkr method. *Chemical Physics*, 348:187–194, 2008.

[77] D. Loureiro. High-temperature modeling of transport properties in hypersonic flows. Master's thesis, Instituto Superior Técnico, 2015.

[78] C. Park. Assessment of two-temperature kinetic model for ionizing air. *Journal of Thermophysics and Heat Transfer*, 3:233–244, 1989.

[79] E. Josyula, W. F. Bailey, and C. J. Suchyta. State-specific dissociation modeling in hypersonic blunt body flow. AIAA Paper 2009- 1579, 2009.

Appendix A

Physical Models

A.1 Thermodynamic Relations

A.1.1 Composition variables

There are several different ways of describing the composition of a chemically reacting gas mixture, meaning how much of species s is present in the mixture. One of these quantities is the number of particles of each chemical species s contained in a volume of the gas, which can be defined by the number density N_s (particles/m^3) or by the the molar density N_s (mol/m^3) of species s, with the two being related through the Avogadro constant N_A. Based on the definitions of N_s and N_s, the following relations hold for the molar density N and the global number density n:

$$N = \sum_s N_s \quad \text{and} \quad n = \sum_s N_s \quad \text{with} \quad N_s = \frac{N_s}{N_A} \tag{A.1}$$

The mass density of each species ρ_s (kg/m^3) can be obtained as follows, if the species particle mass m_i (kg) or molar mass M_i (kg/mol) are known:

$$\rho_s = N_s m_i \quad \text{or} \quad \rho_s = N_s M_i \quad \text{with} \quad m_i = \frac{M_i}{N_A} \tag{A.2}$$

The mixture density ρ is given by:

$$\rho = \sum_s \rho_s \tag{A.3}$$

using the previous quantities, one can define the species dimensionless composition variables mass fraction c_s and molar fraction x_s:

$$c_s = \frac{\rho_s}{\rho} \quad \text{and} \quad x_s = \frac{N_s}{N} = \frac{N_s}{n} \quad \text{with} \quad \sum_s c_s = \sum_s x_s = 1 \tag{A.4}$$

As mentioned before, the composition of the gas may be defined using different quantities. As such, it is possible to establish the following relations between the several composition variables:

$$x_s = \frac{Mc_s}{M_i} \qquad N_s = \frac{x_s \rho}{M} \qquad c_s = \frac{n_s M_s}{\rho} \tag{A.5}$$

where M is the global mixture molar mass, which is obtained by:

$$M = \sum_s x_s M_i = \left(\sum_s \frac{c_s}{M_i} \right)^{-1} = \frac{1}{n} \sum_s N_s M_i \tag{A.6}$$

A.1.2 Equation of State

In this work we are dealing with a multi-component reacting mixture in which the intermolecular forces are considered to be negligible, which means that each individual species s is assumed to behave as an ideal gas. Hence, the total pressure of the mixture P is defined by Dalton's Law as the summation of the partial pressures associated to each species p_s:

$$P = \sum_s p_s \tag{A.7}$$

Also, the perfect-gas equation of state holds individually for each species s, allowing the calculation of the partial pressures using one of the various forms of the equation:

$$p_s = \rho_s R_i T_{tra,s} \quad \text{or} \quad p_s = N_s k_B T_{tra,s} \quad \text{or} \quad p_s = N_s R_u T_{tra,s} \tag{A.8}$$

where R_i is the specific gas constant for the species s, k_B is the Boltzmann constant and R_u is the universal gas constant, which can be related by:

$$r_i = \frac{R_u}{m_s} = \frac{k_B}{m_s} \quad \text{and} \quad k_B = \frac{R_u}{N_A} \tag{A.9}$$

A.2 Thermodynamic Properties

A.2.1 Internal energy

The specific internal energy of the system ε represents the total energy stored in the internal degrees of freedom of all the chemical species that compose the mixture, per unit of mass, and it is given by:

$$\varepsilon = \frac{E}{M} = \sum_s \varepsilon_s c_s \tag{A.10}$$

where E is the total internal energy of the system, M the total mass, ε the specific internal energy of species s and c_s the mass fraction of the species s.

The specific internal energy associated to each chemical species ε_s is defined by:

$$\varepsilon_s = \Delta h_s^o + \varepsilon_{tra,s} + \varepsilon_{rot,s} + \varepsilon_{vib,s} + \varepsilon_{exc,s} \tag{A.11}$$

where Δh_s^o is the standard formation enthalpy, and the terms $\varepsilon_{tra,s}$, $\varepsilon_{rot,s}$, $\varepsilon_{vib,s}$, $\varepsilon_{exc,s}$ correspond to the energies of the different thermal energy modes $\varepsilon_{k,s}$ associated with each species.

A.2.2 Enthalpy

Tthe specific enthalpy h of the gas is defined as:

$$h = \varepsilon + \frac{P}{\rho} \tag{A.12}$$

In the case of a multi-component mixture, similarly to Eqs. A.10 and A.11, the definition of enthalpy can be generalized as follows:

$$h = \sum_s c_s h_s \tag{A.13}$$

$$h_s = \varepsilon_s + \frac{P_s}{\rho_s} \quad \text{or} \quad h_s = \varepsilon_s + r_s T_{tra,s} \tag{A.14}$$

Considering the different internal energy modes:

$$h_s = \Delta h_s^o + h_{tra,s} + h_{rot,s} + h_{vib,s} + h_{exc,s} \tag{A.15}$$

A.3 Multi-Temperature Definitions

This section presents a more detailed definition of the thermodynamic properties of the gas according to a multi-temperature approximation. If thermal nonequilibrium is considered, the global internal energy ε_k associated to each global temperature T_k of the mixture is given by:

$$\varepsilon_k = \sum_s c_s \varepsilon_{k,s} \tag{A.16}$$

In this approach, the amount of energy $\varepsilon_{k,s}$ stored in each energy mode k for a given chemical species s is defined statistically as function of the corresponding temperature $T_{k,s}$ using a Boltzmann distribution. For the vibrational energy mode, a Treanor distribution is preferred, since it allows convergence to an analytic expression.

$$\varepsilon_{tra,s} = R_s T_{tra,s} \frac{3}{2} \tag{A.17a}$$

$$\varepsilon_{rot,s} = R_s T_{rot,s} \tag{A.17b}$$

$$\varepsilon_{vib,s} = R_s \frac{\theta_{vib,s}}{\exp\left(\dfrac{\theta_{vib,s}}{T_{vib,s}}\right) - 1} \tag{A.17c}$$

$$\varepsilon_{exc,s} = R_s \frac{\sum\limits_{s}^{\infty} \theta_{exc,i,s}\, g_{i,s}\, \exp\left(-\dfrac{\theta_{exc,i,s}}{T_{exc,s}}\right)}{\sum\limits_{s}^{\infty} g_{i,s}\, \exp\left(-\dfrac{\theta_{exc,i,s}}{T_{exc,s}}\right)} \tag{A.17d}$$

where $\theta_{vib,s}$ is the species characteristic vibrational temperature, $\theta_{exc,i,s}$ is the characteristic electronic temperature and and $g_{i,s}$ is the degeneracy of the s-th energy level of the species. The ∞ symbol represents the highest achievable energy level before ionization, although, in practice, a finite number of electronic levels may be considered, according to the order of magnitude of the energy exchanges present in the flow. The equations for the rotational $\varepsilon_{rot,s}$ and vibrational $\varepsilon_{vib,s}$ modes apply only to the particular case of diatomic molecules.

The global enthalpy h_k associated to each temperature T_k is given by:

$$h_k = \sum_s c_s h_{k,s} \tag{A.18}$$

and the enthalpy for each thermal energy mode will be defined as:

$$\begin{cases} h_{tra,s} & = \varepsilon_{tra,s} + R_s T \\ h_{rot,s} & = \varepsilon_{rot,s} \\ h_{vib,s} & = \varepsilon_{vib,s} \\ h_{exc,s} & = \varepsilon_{exc,s} \end{cases} \tag{A.19}$$

The component $R_s T$ is only considered in the translational enthalpy since the translational motion is the microscopic mechanism responsible for pressure force.

The gas specific heat at constant volume Cv and the specific heat at constant pressure Cp are defined as the rate of change of the internal energy and enthalpy, respectively, as a function of the temperature:

$$Cv \equiv \frac{\partial \varepsilon}{\partial T} \quad \text{and} \quad Cp \equiv \frac{\partial h}{\partial T} \tag{A.20}$$

In the multi-temperature approach, the previous definitions become:

$$\begin{cases} Cv_k & = \frac{\partial \varepsilon_k}{\partial T_k} \\ Cp_k & = \frac{\partial h_k}{\partial T_k} \end{cases} \quad \text{and} \quad \begin{cases} Cv & = \sum\limits_k Cv_k \\ Cp & = \sum\limits_k Cp_k \end{cases} \tag{A.21}$$

Introducing Eqs. A.16 and A.18 into equation A.21 we obtain:

$$\begin{cases} Cv_k & = \sum\limits_s \left(c_s \frac{\partial \varepsilon_{k,s}}{\partial T_{k,s}} + \varepsilon_{k,s} \frac{\partial c_s}{\partial T_{k,s}} \right) \\ Cp_k & = \sum\limits_s \left(c_s \frac{\partial h_{k,s}}{\partial T_{k,s}} + h_{k,s} \frac{\partial c_s}{\partial T_{k,s}} \right) \end{cases} \tag{A.22}$$

In this equation, we can identify a frozen component, i.e., the specific heats considering a constant chemical composition of the gas, and a reactive component, associated with the heat exchange due to the chemical reactions. The global frozen specific heats at constant volume Cv_k^{f} and at constant pressure Cp_k^{f}, of associated to each temperature T_k are defined as:

$$\begin{cases} Cv_k^{\mathrm{f}} = \sum\limits_s c_s Cv_{k,s}^{\mathrm{f}} \\ Cp_k^{\mathrm{f}} = \sum\limits_s c_s Cp_{k,s}^{\mathrm{f}} \end{cases} \quad \text{with} \quad \begin{cases} Cv_{k,s}^{\mathrm{f}} = \frac{\partial \varepsilon_{k,s}}{\partial T_{k,s}} \\ Cp_{k,s}^{\mathrm{f}} = \frac{\partial h_{k,s}}{\partial T_{k,s}} \end{cases} \tag{A.23}$$

Throughout this work only the frozen component of the specific heat coefficients are used, without any approximation. For simplicity the symbols Cv and Cp are used to refer to the frozen components. Using the frozen definitions, and Eqs. A.15 and A.17 the specific heats associated to the internal energy modes of each chemical species are given by:

$$\begin{cases} Cv_{tra,s} & = \frac{3}{2} R_s \quad \text{and} \quad Cp_{tra,s} = \frac{5}{2} R_s \\ Cv_{rot,s} & = Cp_{rot,s} = R_s \\ Cv_{vib,s} & = Cp_{vib,s} = \frac{\partial \varepsilon_{vib,s}}{\partial T_{vib,s}} \\ Cv_{exc,s} & = Cp_{exc,s} = \frac{\partial \varepsilon_{exc,s}}{\partial T_{exc,s}} \end{cases} \tag{A.24}$$

The specific heats relate to the global R and species R_s gas constants and the specific heat ratio γ by:

$$R_s = Cp_{tra,s} - Cv_{tra,s} \quad \text{and} \quad \gamma = \frac{Cp}{Cv} \tag{A.25}$$

Appendix B

Internuclear Distances of N$_2$ Vibrational Levels

Table B.1: Internuclear distances r_v^{AB} for the N$_2$ vibrationally excited molecule (presented in Å), using the method described in [76]

v	r(v)	v	r(v)	v	r(v)
0	1.10010	21	1.22342	41	1.41880
1	1.10516	22	1.23035	42	1.43453
2	1.11033	23	1.23739	43	1.45158
3	1.11561	24	1.24465	44	1.47006
4	1.12089	25	1.25202	45	1.49020
5	1.12617	26	1.25961	46	1.51253
6	1.13167	27	1.26743	47	1.53750
7	1.13717	28	1.27557	48	1.56588
8	1.14278	29	1.28404	49	1.59856
9	1.14839	30	1.29273	50	1.63739
10	1.15411	31	1.30175	51	1.68447
11	1.15995	32	1.31121	52	1.74322
12	1.16589	33	1.32100	53	1.81660
13	1.17194	34	1.33123	54	1.90361
14	1.17799	35	1.34190	55	1.99789
15	1.18415	36	1.35301	56	2.09580
16	1.19042	37	1.36478	57	2.19910
17	1.19680	38	1.37711	58	2.31307
18	1.20329	39	1.39020	59	2.44739
19	1.20989	40	1.40395	60	2.62231
20	1.21660				
r_{eq}^{AB}	1.0977	σ_{eq}^{AB}	3.798		

Appendix C

SPARK

C.1 SPARK Inputs

As illustrated in Fig. 3.1, in order to run a simulation in code SPARK, an input file is required. The following parameters must be defined:

- `Simulation_Type` - Sets the type of simulation to be performed: 2D axissymetric.
- `Flow_Type` - Sets the flow type and the corresponding set of equations to be solved: Euler, Navier-Stokes.
- `Gas_Model` - Sets the model which describes the behaviour of the gas: nonequilibrium gas.
- `Solver` - Sets the numerical method used to solve the previously established set of equations.
  –`Time_Discretization` - Explicit or Implicit
  – `CFL` - Courant number (depends on the type of simulation being considered and ensures stability)
- `Gas_State` - Sets the upstream conditions.
  – `Pressure` = 27 Pa
  – `Temperature` = 300 K
  – `Mach` = 19.82
  – `Mass_Fractions`: N_2:1
- `Kinetic_Scheme` - Sets the kinetic scheme to be considered: Air5-STELLAR, Air5-STELLAR-Boltzmann.
- `Multi_Temperature` - Sets the parameters required in case the multi-temperature model is being considered (Park's two-temperature model is used in the present work).
  – `Vibrational_nonequ_model` - Individual
  - `Vibrational_nonequ_species` - N2
- `Transport_model` - Sets the transport model being considered: Wilke (Section 2.5.1), Gupta (Section 2.5.2) or STS (Section 2.5.2).